USGS Award G18AP00061: River knickpoint paleogeodesy and measurement of crustal deformation in the Central Virginia Seismic Zone (CVSZ) and Reading Lancaster Seismic Zone (RLSZ).

Frank J. Pazzaglia
Earth and Environmental Sciences
Lehigh University
1 West Packer Ave
Bethlehem, PA 18015
610.758.3667; 3677 FAX; fjp3@lehigh.edu

01 July, 2018 – 30 June, 2019, no-cost extension to 30 June, 2020.

Executive Summary

Geomorphic studies in the Reading-Lancaster seismic zone (RLSZ) and central Virginia seismic zone (CVSZ) focus on paleo-geodetic geomorphic markers such as river terraces, transient knickpoints, catchment-wide erosion rates, channel response times, and the predicted elevation of steady-state channel profiles to document non-uniform rock uplift as a measure of persistent, accumulated crustal strain due to fault slip. These measures directly address two critical knowledge gaps particularly acute in the plate interior setting of the central and eastern US (CEUS): (1) lack of a long-term fault slip time series in zones of known seismicity and (2) known locations of locked seismogenic faults with no historic slip history. For (1), this study shows that the crust has been deformed, and there is a topographic or geomorphic record of non-uniform rock and surface uplift in both the CVSZ and RLSZ. Insofar that this deformation aligns with known structural or geologic features, it is concluded that plate tectonic stresses are generating focused strains that rupture favorably-oriented faults that may have multiple century to millennial-scale recurrence intervals. For (2), this study demonstrates that locations of known, historic seismicity generates a rock and uplift signal that is discernible from the background noise of rock-erodibility and transience in the channel-hillslope system for catchments that share the same base level fall history. As a result, the methods and approach described in this research is portable to other parts of the CEUS as a tool to discover locked, but seismogenic faults that have a pre-historic slip record.

Project Report

1. Introduction

1.1 Goal of Investigation

Intraplate seismicity presents a particularly difficult problem in the effort to mitigate hazards in the central and eastern U.S. (CEUS) where the nation's infrastructure is brittle because of widespread non-reinforced masonry construction, age, and decades of deferred maintenance. Even though large historic earthquakes in the CEUS have been few, they have been damaging, as was the case for Charleston, S.C. in 1886 (Mw 7) and to a lesser degree, Mineral, Virginia in 2011 (Mw 5.7). The most recent August, 2020 Sparta, NC earthquake (Mw 5.1) just reinforces the point that even modest-sized earthquakes in the CEUS can have broad impacts.

The most densely populated corridor in CEUS lies in the mid-Atlantic region, following the Fall Zone and extending westward across the Appalachian Piedmont to the foot of the Blue Ridge. Embedded in this region are the central Virginia seismic zone (CVSZ) and Reading-Lancaster seismic zone (RLSZ; **Fig. 1**). Several of the largest, most widely-felt earthquakes in the mid-Atlantic region nucleated in these seismic zones including the 2011 Mineral, VA earthquake, the 1994 M 4.6 Sinking Spring, PA earthquake, and the 1984 M 4.2 Lancaster County, PA earthquake, all with epicenters located 23, 38, and 21 km respectively from the nearest operating nuclear power generating station. None of those stations were damaged by earthquake ground accelerations, but as the population density increases and we continue to invest in our energy generation to meet rising demands, the need for **novel geologic inputs capable of improving the National Seismic Hazard Model (NSHM) for urban areas** will grow. Specifically, this proposal targets the need *to identify seismic sources* (faults) *and seismic potential in CEUS using geologic and paleogeodetic data*, that have driven crustal deformation, and which may or may not be directly associated with seismicity.

This research is inspired by work started with colleagues at Lehigh, the USGS, and the State of Virginia following the Mineral earthquake and initially funded by a USGS EDMAP (G13AC00115) and USGS EHP award (G15AP00092). The overall effort seeks to use geomorphic paleogeodesy as a way of locating seismogenic faults and co-seismic surface deformation as a guide to traditional paleoseismic analysis of trenching for calculating paleo-earthquake magnitudes and recurrence intervals. Geomorphic markers, including knickpoints that decorate river longitudinal profiles (c.f. Marple and Talwani, 2000; Berti et al., 2015), represent *(paleo)geodetic data* that integrate crustal strains over geologic time scales, and can be used to develop *novel methodologies to improve slip rate estimates along faults or across regions, and reconstruct recurrences of earthquakes for application to seismic hazard analysis, also contributing to a priority topic for National Research (NAT),* in addition to the CEUS.

Integrating geodetic information over long time scales using geomorphic markers is one way

to avoid the problem of identifying crustal strains, particularly if they are transient, in the absence of or as a complement to observed seismicity. In this context, the goals of this research are to align with the ***CEUS and NAT priority topics of providing novel geologic, geomorphologic, and paleogeodetic inputs capable of improving slip rate estimates across faults in known regions of intraplate seismic activity, reconstruct recurrences of earthquakes for application to seismic hazard analysis, and contribute to improving the NSHM.*** Encouraged by the success realized by the now completed USGS EHP (G15AP00092) project, the research seeks to use knickpoints, cosmogenically-measured catchment erosion rates, the response times of longitudinal profiles to non-steady rock uplift, and a prediction of steady-state channel elevation using the stream power erosion rule for bedrock channels in the mid-Atlantic Piedmont as geomorphic markers. These markers will be used to measure slow, but persistent accumulation of intraplate stresses capable of triggering earthquakes on favorably-oriented new or legacy faults.

1.2. Project Personnel and Products

This project supported the M.S. Thesis of Joshua Gonzales at Lehigh University (Gonzales, 2019). It also provided partial support for an undergraduate senior research project by Boo-Kyo Sur, who served as Joshua's field assistant in the summer of 2018. Analysis of geochronology data presented in this report was mentored by Lee Corbett and Paul Bierman at the Community Cosmogenic Laboratory at the University of Vermont. The overall project mentor for the students and project Principal Investigator was Frank J. Pazzaglia. To date, the following abstracts and journal articles have been supported by this research:

Gonzales, J. M., Pazzaglia, F. J., and Sur, B., **2018**, Using knickpoints as geomorphic markers of crustal deformation in a seismically active intraplate setting: Abstract [EP53E-1947] presented at 2018 Fall Meeting, AGU, Washington D.C., 10-14 Dec.

Gonzales, J. M., **2019**, Using knickpoints as geomorphic markers of crustal deformation in Appalachian Piedmont seismic clusters: MS Thesis, Bethlehem, PA, Lehigh University, 87 p.

Gonzales, J. Pazzaglia, F. J., Anastasio, D. J., Germanoski, D. Gallen, S. F., Corbett, L. B., Bierman, P. R., and Caffee, M. W., **2020**, Crustal strain in the Pennsylvania Piedmont revealed by long profile modeling and its relation to active seismicity: Geological Society of America Abstracts with Programs, 52, 6, doi: 10.1130/abs/2020AM-358491.

Pazzaglia, F.J., Malenda, H.F., McGavick, M. L., Raup, C., Carter, M.W., Berti, C., Mahan, S., Nelson, M., Rittenour, T.M., Counts, R., Willenbring, J., Germanoski, D., Peters, S. C., and Holt, W.D., **in press**, River terrace evidence of tectonic processes in the eastern North American plate interior, South Anna River, Virginia: Journal of Geology, 000, 000-000.

Gonzales, J. and Pazzaglia, F. J., **in prep**, River channel paleogeodesy and intraplate deformation in the eastern US : to be submitted to Geological Society of America Bulletin.

1.3. Outline of Report

This report will first establish the relevant scholarly background for intraplate seismicity and crustal strains specific to CEUS. It will identify the knowledge gaps and how this EHP research was positioned to make progress in addressing one or more of these knowedge gaps. It will then lay out the rationale for using geomorphic markers as a measure of crustal strains in slowly-deforming intraplate settings. The report will then follow a standard outline of describing the study areas, the methods employed, the data collected, and interpretations of those data. It will conclude with a brief assessment of challenges encountered, how successful we were at meeting original proposal expectations, and opportunities for future research.

2. Background

2.1. Intraplate seismicity and the challenges presented by slow rates of deformation

Crustal deformation in continental plate interiors is neither well described nor understood by plate tectonics which has been constructed primarily to explain observations at plate margins (McKenzie and Parker, 1967; Morgan, 1968; Gordon, 1998; Subarya et al., 2006; McCaffrey, 2009). Yet we know that continental interiors deform because we observe earthquakes, some large and damaging (Baljinnyam et al., 1993; Tuttle et al., 2002; Liu et al., 2011; Wolin et al., 2012; King et al., 2019), deformed stratigraphic and geomorphic markers (Berti et al., 2015; Rovere et al., 2015; Van Arsdale et al., 2019), and GPS-geodetic strain (e.g. Calais and Stein, 2009; Sella et al., 2007; Argus and Peltier, 2010) far from plate boundaries. A major challenge in the study of intraplate tectonics is the short earthquake catalog and the long recurrence interval of major seismic events that stem from the low strain rates typical of intraplate regions (<<1mm/ yr; Calais et al., 2006). Modern seismicity maps are but a snapshot of a process that occurs over thousands of years, rendering historic seismicity an incomplete sample of a much longer-term process. Coupled with the observation that intraplate seismogenic faults commonly do not create an easily identifiable morphological signature, traditional hazard estimation that relies on location and size of sources, and estimates to rupture at repeat times are compromised (McCalpin, 2009).

The general lack of easily-identifiable surface ruptures (c.f., King et al., 2019) further hampers the effort in finding seismogenic faults in plates interiors. As challenges in precisely locating low-magnitude seismicity have recently been overcome (Wu et al., 2015; Chapman et al., 2016; Soto-Codero et al., 2018), seismology remains a primary way to find and characterize intraplate seismogenic faults. As a result, construction of seismic hazards maps continues to rely heavily on observable seismicity. However, the transient or persistent nature of observed seismicity is difficult to characterize from short instrument records, and stresses could also be accumulating on locked, but aseismic structures. Examples of these problems have been discussed for both intraplate (Ebel, 2009; Stein and Liu, 2009; Liu et al., 2011) and plate boundary settings (Stein et al., 2012).

One way to address the problems of the transient, or persistent, or nonuniform distribution of earthquake-causative stresses in ENAM comes from an emerging class of geodynamic models that incorporate geophysical observations of crustal and lithospheric structure (Schmandt and Lin, 2014; Biryol et al., 2016; Shen et al., 2016; Aragon et al., 2017; Long et al., 2017; 2019; Soto-Cordero et al., 2018) and also link solid Earth and Earth surface processes (Moucha and Ruetenik, 2017). For example, the stresses generated by a steady-state, fully coupled, vertically integrated plate tectonics geodynamic model (Ghosh et al., 2013; 2019) predicts a focused surface strain field in ENAM co-located with the central Virginia seismic zone (CVSZ). These results suggest that CVSZ earthquakes are being driven by persistent tectonic stresses, perhaps localized by lithospheric heterogeneities inherited from ENAM formation and evolution. The model predictions also suggest that the tectonic signal of crustal deformation should be resolvable above the background noise of other vertical and horizontal crustal motions such as geodetically derived glacial isostatic adjustment (GIA) (Muir-Wood, 2000; Sella et al., 2007; Peltier et al., 2015; Pritchard and Yun, 2015). This class of models has fully articulated components and couplings (Willett et al., 2006; Turcotte and Schubert, 2014) and predictive capabilities that can be tested (Rouet-Leduc et al., 2017; Hulbert et al., 2019).

2.2. Assessing hazards from intraplate seismicity

Deciding where large earthquakes are likely is an additional challenge (Ebel, 2009; Stein and Liu, 2009; Liu et al., 2011; Brooks et al., 2019; Salditch et al., 2020) further complicated by the slow intraplate strain rates. As beautifully laid out in a recent paper by Salditch et al. (2020), a long-standing guiding assumption has been that future seismicity is more likely to take place where current seismicity is occurring because faults are locked, accumulate strain in the interseismic period, release that strain co-seismically during earthquakes, and have no memory (Reid, 1910). Periodic earthquakes are predicted by these assumptions and modeled using a Poisson approach. Of course many subsequent observations have pointed out that faults may have a short-term memory of strain accumulation leading to variable release during earthquakes and generating aperiodic clusters of seismicity (Shimazaki and Nakata, 1980; Wallace, 1987), all of which has led to other statistical modeling approaches to predict future seismicity (Salditch et al., 2020).

Collectively, application of any model to intraplate fault slip and seismic hazards are hampered by two critical knowledge gaps particularly acute in plate interiors: (1) long-term time series of fault slip and (2) known locations of seismogenic faults. As illustrated by large, but infrequent intraplate earthquakes in the central and eastern United States (CEUS), the seismic hazard map changes shortly following an earthquake, whether it be New Madrid (1811-12), Charleston (1886), Mineral, VA (2011), or Sparta, NC (2020), all of which ruptured previously unknown faults.

This report summarizes an approach for addressing these problems and partially closing the knowledge gaps that also may test the predictions of the intraplate geodynamic models. We

integrate paleo-geodetic information over long time scales using geomorphic markers as a way to identify crustal strains that accumulate slowly. The long integration time of geomorphic markers provides a means to discern persistent crustal deformation from transient geodetic noise characteristic of instrument time scales or GPE, GIA, or flexural isostatic mechanisms. Furthermore, geomorphic markers offer the possible benefit of identifying crustal strains in an intraplate setting not otherwise identified by observed seismicity.

2.3. Conceptual approach in using geomorphic markers in intraplate settings

Our conceptual approach is to study the longitudinal profiles of rivers in ENAM, in two settings where there has been historic seismicity, to discern if the steepness of the long profiles, transient features like knickpoints, catchment-wide erosion rates, and predictions of the steady state elevations of river channels by the well-accepted stream power erosion rule is capable of measuring crustal strain that has accumulated over long periods of time, and has been recorded topographically recorded as non-uniform rock uplift (**Fig. 2**). Where possible, the long profile data can be compared and constrained by depositional geomorphic or stratigraphic markers including river terraces and Coastal Plain deposits.

This research focuses on the response times of the long profiles to base level fall (uplift) as a long-term, integrative paleogeodetic recorder of plate interior crustal deformation. Specifically, we focus on transient knickpoints (**Fig. 2**), which have been successfully used to measure crustal strains in tectonically active settings, particularly when they can be independently downstream correlated to and dated with deposits such as marine terraces (Pavano et al., 2016). Knickpoints are locally steep reaches (convexities) in an otherwise typically concave-up graded river longitudinal profile that may be present due to non-uniform lithology or as transient features of fluvial adjustment to changes in base level (Whipple and Tucker, 1999). Transient knickpoints may be modeled as a kinematic wave that migrates headward through a watershed following an impulsive base level fall (Whipple and Tucker, 1999; Crosby and Whipple, 2006; Berlin and Anderson, 2007). Because the crest of this wave, essentially the upper lip of the knickpoint, maintains a constant vertical velocity climb through the topography in rocks of equal or comparable erodibility, (Niemann et al., 2001), variable elevation of isochronous knickpoints rocks may be interpreted in terms of crustal deformation (Miller et al. 2013; Pavano et al., 2016).

Knickpoints are common in landscapes, easy to identify in rivers using long profile analyses (Snyder et al., 2000; Perron and Royden, 2013), and the celerity of their headward propagation through watersheds can be modeled if substrate erodibility and landscape erosion can be constrained. High-resolution topography, coupled with terrestrial cosmogenic nuclide (TCN) dating of nested watershed erosion rates, and field-based rock erodibility measurements (Murphy et al., 2018; Shobe et al., 2017) provides our basis for modeling knickpoint and long profile evolution, taking advantage of computational tools in the MATLAB-based TopoToolbox suite (Schwanghart and Scherler, 2014). Component details of longitudinal profiles and our modeling approach are fully described below in the Methods section.

3. Study Areas

3.1. CVSZ – South Anna River

The CVSZ study area is located in Louisa County, Virginia, in the Appalachian Piedmont geologic and physiographic province ~65 km northwest of Richmond and ~150 km south of Washington D.C. (**Fig. 3**). Elevations here range from ~50 m for the valley bottoms to ~150 m for the interfluves where a rolling upland with 10-20 m of relief contrasts with locally steep, incised river valleys. The South Anna River is positioned between the James and Rappahannock rivers that flow southeast across the Virginia Piedmont towards the Atlantic (**Fig. 3**). With headwaters arising in the western Piedmont at an elevation of ~305 m, the South Anna River flows southeast for ~160 km before crossing the Fall Zone north of Richmond and joining the North Anna River at Ashland, VA to become the Pamunkey River/Estuary in the Coastal Plain, draining in total ~1,025 km^2.

The Piedmont in Virginia is a Paleozoic amalgamation of complex terranes and structures varying in age, sutured to North America, and deformed during the building of the Appalachian Mountains. Major associated structures are contractional and translational thrust and strike-slip faults. Post-orogenic extension, leading to the breakup of Pangea and the opening of the Atlantic Ocean, placed the Piedmont in the lower plate of a major decollement and superposed high-angle Late Triassic and Jurassic normal faults that are thought to both reactivate and cut across the older Paleozoic structures.

The South Anna River basin is underlain by meta-volcanic, volcaniclastic, and igneous rocks of an arc that was accreted and deformed during the early Paleozoic Taconic orogeny (Horton et al., 1989; Pavlides 1989; Hughes et al., 2013). The prevailing structural grain of these rocks is northeast-southwest (**Fig. 3**). In summary, although Piedmont rocks vary in lithology, they are generally deeply weathered at the surface and differences in their erodibilities are assumed to be small.

3.2. Mineral Earthquake

The M_w5.7 Mineral, Virginia earthquake occurred at 17:51:04 UTC (1:51:04 PM EDT) on 23 August 2011. The epicenter of the mainshock was located at 37.905°N, 77.975°W (WGS84), with a focal depth of ~8.0 km (Chapman, 2013; **Fig. 3c**). Slip occurred on an up to the SE reverse fault having a moment tensor solution of N28°E, SE dip of 50°, and rake 113° derived from regional moment tensor inversion (Chapman, 2013 citing Herrmann, 2011). The rapid deployment of instruments following the mainshock resulted in nearly 400 well-recorded and well-located aftershocks of $M_w > 1.8$ (Horton and Williams, 2012; McNamara et al., 2014a,b; Horton et al., 2015) that identified a previously unrecognized 10-km-long rupture zone striking ~N30°E and dipping east-southeast ~45° (Ellsworth et al., 2011) originally termed the Quail fault zone (Horton et al., 2015). Subsequent work using a much larger dataset of ~1600 aftershocks, double-difference location methods, and 393 well-constrained focal mechanisms shows that the

mainshock rupture zone was not illuminated by the aftershock pattern (Wu et al., 2015). Only ~30% of the aftershocks have focal mechanisms similar to the mainshock and instead represent a diffuse zone of Coulomb stress transfer mostly above the mainshock (Wu and Chapman, 2017). The mainshock ruptured a small area probably less than 3 km in diameter and the rupture did not propagate upwards to less than 6 km depth, an observation consistent with the lack of any identifiable surface rupture. Collectively, the seismological evidence indicates that there is a broad zone of variously oriented minor faults at shallow depths above the main rupture, rather than a single fault plane as originally envisioned by the Quail fault.

3.3. RLSZ – Pennsylvania Piedmont astride the Susquehanna River

The Pennsylvania Piedmont is a rolling upland ~100-250 m above sea level that is locally incised by steep, narrow bedrock streams tributary to the Potomac, Susquehanna, and Delaware rivers (**Fig. 4**). The Susquehanna River bisects the Pennsylvania Piedmont study area and marks the western boundary of the RLSZ with no comparable historic seismicity further west in York County. This river, the largest Atlantic slope drainage, carves a 200 m-deep gorge into the High Piedmont slicing through a prominent, northeast plunging topographic ridge called the Westminster Anticline (Campbell, 1929). The opposing tributary streams of Tucquan Creek and Otter Creek fall steeply through these topographic and structural ridges to meet the Susquehanna (**Fig. 4**). Otter Creek is 3.3 km further upstream along the Susquehanna River, but effectively, both tributaries experience the same base level and have a contemporaneous base level history.

Tucquan Creek and Otter Creek are tributaries of comparable drainage area, overall relief, and underlying geology (**Fig. 4b**). Tucquan Creek, the lower section of which is part of a Pennsylvania Wild and Scenic River Preserve, flows primarily SW in a narrow, elongated watershed covering ~ 16.7 km^2, whereas Otter Creek flows primarily SE in larger, wider watershed covering ~ 49.4 km^2. The Otter Creek watershed is distinctly asymmetric with several large tributaries flowing from the south and only few short tributaries entering from the north (**Fig. 4b**). The Tucquan watershed, on the other hand is symmetric, but lacks the normal, characteristic, broad upland catchment shape (**Fig. 4b**). Both streams display increased sinuosity in the steep gorges of their lower reaches, becoming less sinuous as the channels climb into the Piedmont upland. Elevations in these watersheds range from ~60 to 260 m. Both have a distinct, rolling, low-relief Piedmont upland surface that gradually gives way to a more rugged, incised, steep narrow valley towards the Susquehanna River (**Fig. 4b**). The channels alternate from reaches of nearly complete bedrock exposure to mixed bedrock-alluvial where the alluvium is typically < 1 m thick. Regolith and saprolite is more abundant in the upper, low-relief areas of the watersheds whereas bedrock and thin colluvium underlie the hillslopes closer to the Susquehanna River.

The Pennsylvania Piedmont is underlain by amphibolite grade schist, among which is the Octoraro Formation (**Fig. 4**), a lower Paleozoic albite, mica, garnet schist with common quartz veins. These metamorphic rocks exhibit several foliations and jointing consistent with 3 stages of

folding (Freedman et al., 1964; Valentino, 2004; Hill, 2007).   The foliations collectively define a structural feature called the Tucquan anticline that geographically coincides with the topographic Westminster anticline where the former is exposed along the Susquehanna River (**Fig. 4**). The hinge of the Tucquan anticline strikes southwest - northeast through and subparallel to Tucquan Run. The Octoraro Formation comprises the hanging wall of a major Paleozoic thrust called the Martic Line (Knopf and Jonas, 1929; Jonas and Stose, 1930) that places these older, high-grade, deeper water facies over younger, lower-grade carbonate and clastic rocks further north (**Fig. 4**). The rocks and topography north of the Martic line stand lower in elevation, called the Low Piedmont, in contrast to the Piedmont underlain by schist south of the Martic Line and called the High Piedmont.

Otter Creek and Tucquan Creek are the northernmost Susquehanna tributaries wholly within the Octoraro Formation. For comparison, this study also includes eleven other streams that also lie wholly or partially within the Octoraro Formation (**Fig. 4**). One of these, Pequea Creek, is a large stream with a catchment in the Low Piedmont, but also directly through the RLSZ (**Fig. 4**). All of the others, Kelly's Run, Wissler Run, Fishing Creek, Sawmill Run, Counselman Run, Duncan Run, Oakland Run, Mill Creek, and Anderson Creek are of variable size, but all underlain by schist, including variable amounts of Octoraro Fm.

3.4. The 1984 Lancaster earthquake

The 23 April, 1984 Mw 4.2 Lancaster earthquake (Stockar, 1986; Armbruster and Seeber, 1987) ruptured a NNE-trending, steeply east-dipping fault (**Fig. 4**) at a depth of ~ 4.5 km that is discordant to the mapped Paleozoic structures in Lancaster County, but sub-parallel to Mesozoic, Newark Basin, rift-related diabase dikes. The slip on the Lancaster earthquake fault is oblique reverse, with a right-lateral strike-slip component (Stockar, 1986; Armbruster and Seeber, 1987). Both the updip and along strike projection of the Lancaster earthquake rupture predicts distributed crustal deformation, albeit of lesser magnitude, in the core of the Tucquan watershed similar to what has been modeled for the Mineral earthquake in central Virginia.

4. Methods

4.1. Field Approaches

Surficial deposits and soils in a swath ~2 k wide and following ~20 km of the South Anna River valley in the Ferncliff and Pendleton quadrangles, Louisa County, VA were mapped at the 1:24,000 scale in (Malenda et al., 2014; McGavick, 2017). Field data were collected from 2014 through 2017 to determine the rate of modern erosion, define and numerically date the stratigraphy and sedimentology of river alluvium, and describe the soil geomorphology along the main stem of the South Anna River.   The terrace data extends from Byrd Mill to South Anna, VA spanning the surficial extrapolation of the region impacted by the 2011 rupture (**Fig. 3**).

Field data were collected from the trunk channels of Tucquan Creek and Otter Creek (**Fig. 4**) over a three-week period in July 2018, and a one week period in August 2018. The data collection strategy was designed to describe and quantify the erodibility of the substrate, the characteristics of the channel with respect to the rock structure, and the rate of erosion.

4.1.1. Compressive strength and channel orientation measurements

A Schmidt hammer was used to collect measurements of compressive rock strength for bedrock exposures along the stream banks of and protrusions into the stream channel of Tucquan and Otter creeks at approximately 5 m vertical intervals.   The Schmidt hammer measures uniaxial compressive strength through the rebound velocity of a spring-loaded piston after striking a surface. The recorded rebound value (RV) is proportional to the compressive and tensile strength of the material (Murphy et al. 2016). While susceptible to interference from fractures, subsurface fracturing, moisture, and interference from lichen and moss, the Schmidt hammer has been shown to be an effective tool in measuring rock erodibility (see review in Murphy et al., 2016).

In total, 15 sites in Tucquan Creek and 23 sites in Otter Creek were sampled between ~61 - 115 m. Above 115 m, 9 sites in Tucquan Creek and 4 sites in Otter Creek were measured where permitted by bedrock exposure. The crests of the 107 m Erb Mill knickpoint in Tucquan Creek, the 75 m knickpoint in Tucquan Creek, and the 60 m knickpoint Otter Creek were densely sampled from bank to bank. At each sample site the orientation of 1-5 joint and F1 foliation planes were recorded and a minimum of 30 Schmidt hammer measurements were collected parallel to the plane orientations accounting for variations in strike angle, fractures, and vegetative cover.

In addition to the structural measurements, channel-reach orientation were binned and summed for 0.5 km-long segments to assemble the integrated channel length as a function of channel orientation for the trunk channels. This metric, termed the reach-length index (RLI), can be directly compared to joint and foliation orientations to ascertain qualitative coincidence of structural and channel orientations.

4.1.2. Terrestrial cosmogenic nuclide (TCN) sample collection

Terrestrial cosmogenic beryllium-10 (TCN ^{10}Be) in quartz-bearing alluvial deposits is well-established as an effective measurement of spatially averaged upstream basin erosion rates (Brown et al., 1995; Bierman and Steig, 1996; Granger et al., 1996; Matmon et al, 2003; Cyr et al., 2010; Portenga et al., 2013). The sampling protocol involved collecting ~10 kg of naturally washed and sorted sand from sand bars and channel banks during summer low-water conditions. For Tucquan and Otter creeks, this included 14 nested sites along the channel reaches of Tucquan Creek (6 samples) and Otter Creek (7 samples). Samples were collected at the mouth of each stream, above the backwater influence of the Susquehanna River, in tributaries to the creeks within the steep gorges where knickpoints are most visible, and in each tributary just upstream of

major confluences. By nesting samples in this way, differential erosion rates above and below knickpoints, as well as the relative contributions of sediment from the incised lower valley portion vs the upper portion of the watershed can be identified. Bulk channel alluvium samples for [10]Be TCN analysis were washed, dried, and sieved in order to retain grain sizes in the range of 0.125-0.7mm. Quartz was purified and [10]Be extracted at the University of Pennsylvania cosmogenic analysis lab and analyzed at the PRIME accelerator lab at Purdue University.

A similar strategy was employed in the collection of alluvium from the South Anna River main channel and its tributaries. Sample locations were chosen to represent erosion rates near and distal to the epicentral region both upstream and downstream. The sampling sites are also distributed to determine erosion rates above and below a prominent 93 m elevation knickpoint as well as for sub-basins of diverse rock type. Bulk channel alluvium samples for [10]Be TCN analysis were washed, dried, and sieved in order to retain grain sizes in the range of 125-700 μm. Quartz was purified and [10]Be extracted at the University of Pennsylvania cosmogenic analysis lab and analyzed at the PRIME accelerator lab at Purdue University.

Resulting [10]Be concentrations were modeled for erosion rate using the online CRONUS dating calculator (Balco et al., 2008; http://hess.ess.washington.edu/) considering a sample thickness of 0 cm and sample density of 2 g cm^{-3}, chosen to model cosmic ray penetration into soil and saprolite, rather than rock Given the low relief and gentle seaward dip of all of the Piedmont basins, no topographic shielding correction was used in calculating the erosion rates (DiBiase, 2018).

4.1.3 River terraces

River terraces were mapped and described (Malenda et al., 2014; 2015; McGavick, 2017) following traditional field approaches of mapping, section measuring, soil morphologic description, and sampling for sediment composition and deposit geochronology. Data were collected on 1:24,000 scale, 10-ft contour interval paper maps also reproduced on field computers. The topographic data were supplemented further by 10-m SRTM DEM and 1-m resolution LiDAR digital topography publicly available as part of the National Map dataset (https://viewer.nationalmap.gov/basic/?basemap=b1andcategory=ned,nedsrcandtitle=3DEP %20View). Identification of alluvial from residual or colluvial deposits, and a terrace lithostratigraphic model (Malenda et al., 2014; McGavick, 2017) was aided by shallow auguring using a 1-m long, 10-cm wide bucket auger. Deposits containing rounded gravel interbedded with (stratified) sparsely micaceous sand and silt were identified as alluvium, which contrasts with residual soil, colluvium, and saprolite that are dominated by angular gravel, and red, abundantly micaceous, unstratified matrix. Natural exposures of alluvial deposits are restricted almost entirely to the inner meander bends of the South Anna River. These exposures are supplemented by hand-dug pits on the treads of terraces, typically in wide, flat, cultivated fields. A complete geochronologic framework for the river terraces based on luminescence and TCN exposure ages is described in Pazzaglia et al., (in press).

4.2 Longitudinal profile modeling

Topographic and stream planimetric analyses were extracted from publicly available datasets assembled from 1-, 10-, 30-, and 90-m resolution digital elevation models (DEMs) of the Appalachian Piedmont and Inner Coastal Plain (https://viewer.nationalmap.gov/basic/).   These data offer resolutions that can be processed to generate a planimetric river channel network that closely aligns with USGS 1:24,000 scale blue line channels.   MATLAB TopoToolbox 2 (Schwanghart and Scherler, 2014) and ArcGIS were both used to process and analyze the topographic data.   In the South Anna study, five, ~100-km long, 2-km separated adjacent topographic profiles arranged in the direction of river flow (NW-SE) and orthogonal to drainage flow (SW-NE) were used to generate the topographic swaths. The distance between adjacent profiles is about half as wide as the major drainage basins, and this distance insures that the minimum and the maximum elevations of the river valleys and interfluves are captured.

River profile data for streams in the Pennsylvania Piedmont were extracted from a 1-m resolution NED 3-DEP LiDAR DEM, up-sampled to 10-m resolution in an effort to reduce noise from artificial structures that interfere with the hydrologic modeling of flow direction routines. Profiles for streams or parts of streams that flow outside of the Pennsylvania Piedmont, including the South Anna River were extracted from the 10-m NED DEM. DEMs were assembled in ArcGIS 10.x and then analyzed in MatLab using TopoToolbox (Schwanghart and Scherler, 2014). Channels were defined with a minimum upstream drainage area of 1 km^2. Stream network profiles were smoothed using a constrained regularized smoothing routine that forces monotonically downstream decreasing elevation (Schwanghart and Scherler, 2014).

River incision rates, channel elevation, channel steepness, upstream knickpoint (a short but steep channel reach) migration (channel response times), channel projections, and drainage divide stability are all based on longitudinal profiles of the trunk channels and tributaries with > 0.5 km^2 drainage area extracted from the DEMs. The stream power law (Howard and Kerby, 1983; Howard, 1994; Whipple and Tucker, 1999) provides a common point of reference for the comparison of the longitudinal profiles and generation of these metrics,

$$E = KA^m S^n \qquad (1),$$

where channel erosion (E) is the product of rock erodibility (K), drainage area (A), and slope (S), the latter of which have power dependencies, m and n. Longitudinal profile slopes have a power-law decrease with increasing drainage area, defining Flint's Law (Flint, 1974; Hack, 1957; Morisawa, 1962),

$$S = k_s A^{-\theta} \qquad (2),$$

where k_s is the y-intercept of (2) and defined as the profile steepness, and θ is the slope of the

regression through the S-A data and defined as profile concavity. Assuming steady drainage basin area (fixed divides) and a rate of rock uplift balanced by the rate of erosion, equations (1) and (2) can be combined and solved for local slope. Doing so shows that k_s scales with the rate of rock uplift, given a similar rock erodibility (K; Snyder et al., 2000; Kirby and Whipple, 2001, 2012; Lague, 2013),

$$k_s = (U/K)^{1/n} \tag{3}.$$

Because θ and k_s co-vary, it has become common practice to chose a reference concavity (θ_{ref}) for all of the streams in the watershed, resulting in a normalized k_s value (k_{sn}). The value of -0.45 is commonly chosen for θ_{ref} based on both theory and observation. When a linear power dependency for the slope term ($n=1$) is considered, a reasonable simplification for the detachment-limited, plucking-dominated erosion process in mixed bedrock-alluvial channel Piedmont streams (Miller et al., 2013; Whipple et al., 2013; Gallen, 2018; Gallen and Thigpen, 2018), equation (4) reduces to a simple relationship between uplift (or erosion for the steady-state case), rock erodibility, and profile steepness. In the case where n=1, and $\theta=$-0.45, the units on k_s are $m^{0.9}$.

By combining equations (2) and (4) a description for the response time (τ, Whipple and Tucker, 1999) of the South Anna River to a downstream base level change is derived,

$$\tau(x) = \int_0^x \frac{dx'}{K(x') A(x')^n} \tag{4},$$

where x' is the incremental distance in x. Equation (4) describes the amount of time it takes for a transient erosional step (a knickpoint) to move up the long profile as a kinematic wave. Similarly, substituting dz/dx for S in equation (2), solving for dz, and then integrating arrives at an expression for predicted channel elevation $z(x)$:

$$z(x) = z(x_b) + \int_{x_b}^x k_{sn}(x') A(x')^{-\theta} dx' \tag{5},$$

where x_b is the starting base level elevation. For $\tau(x)$ and $z(x)$, this analysis uses K values that depend on a long-term rate of uplift (and erosion) measured cosmogenically and mean k_{sn} that are calculated in three ways: (1) using the step-wise median determined by equation (2) and applied across all watersheds as a single, average or median value (Model 1), (2) using the step-wise mean determined by equation (2) and applied as a single median value per watershed (Model 2), and (3) a mutual linear inversion of all channels for k_{sn} (Gallen, 2018) with an upstream drainage area ≥ 0.5 km^2 and averaged over 10 m elevation intervals (Model 3). Mean k_{sn} at the TCN

sampling locations is achieved by averaging all of the 10-m (nominally) pixel k_{sn} values upstream of the sampling location, using a reference concavity (θ_{ref}) of 0.45. Application of equation (3) allows a linear regression through these data on a log-log plot where the slope of the regression is $1/n$, and the y-intercept is $(1/K)^{1/n}$.

A complementary way to visualize gradient and elevation difference among channels is the χ (chi) linear transformation of stream long profiles (Harkins et al., 2007; Perron and Royden, 2013)

$$\chi = \int_{x_b}^{x} A(x')^{-\theta} dx' \qquad (6).$$

This metric identifies where adjacent streams are flowing in basins of disparate elevations and thus poised to capture or to be captured (Willett et al., 2014). The χ metric is particularly useful for the visualization of disequilibrium in channel-head elevation and stream power across a drainage divide (Harkins et al., 2007; Whipple et al., 2017). In making the regional steepness and χ maps, we assume a θ_{ref} of -0.45.

Equations (5) and (6) can be combined and recast to describe the base level fall history of a steady-state catchment, assuming that the uplift is uniform and the base level fall occurs only at the mouth of the stream, which does not change over time (Goren et al., 2014; Gallen 2018). Under these conditions, eq. (5) reduces to

$$z(0,x) = \int_{-\tau(x)}^{0} U(t') dt' \qquad (7).$$

This equation states that at all points in x (channel distance) that have the same response time, will also have the same elevation. This is an expression of transient knickpoints, moving as kinematic waves through catchments do not necessarily need to experience uniform rock uplift and in this case, equation (5) predicts that

$$\frac{dz(x)}{d\tau} = U(x) \qquad (8).$$

Combined with equation (6), Goren et al. (2014) show that the block uplift scenario (eq 7) becomes

$$z(0,x) = \int_{-\chi(x)}^{0} U*(t') dt' \qquad (9),$$

and the non-uniform solution (eq. 8) becomes

14

$$\frac{dz(x)}{d\chi} = U*(x) \tag{10},$$

where U* is a non-dimensional uplift term. Equations (9) and (10) form the basis of a matrix linear inversion technique where the equations can be organized as

$$A*U = z \tag{11},$$

where $A*$ is an N x q matrix where q is the number of time intervals. The full derivation of the inverse technique is described in Goren et al. (2014) and several MatLab codes have been developed subsequently to execute it (Gallen, 2018). These codes are used here in reconstructing the base level fall histories for catchments in the Pennsylvania Piedmont.

All of the equations presented here are predicated on a constant drainage area (A) for modeled catchments, an assumption that is probably false for at least some of the catchments. Unknowable changes in the area term over time will introduce an unknown amount of uncertainty into the model calculations. The analysis proceeds on the assumption that the change in drainage area has been small over the past several million years so the degree of uncertainty in applying equations above will also be correspondingly small.

Independent estimates on knickpoint age is accomplished by projecting the upper, concave reaches of the profiles above the knickpoints downstream through the current incised reach to the Fall Zone using equation (2). Here, the projected profiles intersect terraces and upland gravels of known age (Pazzaglia, 1993; Pazzaglia and Gardner, 1993; Weems et al., 2012; Pazzaglia et al., in press). The knickpoint age is taken to coincide with the initiation of the base level fall since the deposition of the terrace or upland gravel.

5. Results

5.1. CVSZ – South Anna River

The longitudinal profile of the South Anna River (**Fig. 5**) is segmented, beginning as a stepped, but mostly concave reach in the headwaters and continuing downstream for ~35 km through the Potomac terrane and Ellisville Granodiorite to a prominent, ~4 m high bedrock knickpoint and waterfall at Byrd Mill. This knickpoint is within the Potomac terrane and its top is at an elevation of 93 m. Less than a kilometer downstream the profile passes into the Chopawamsic Fm with no change in gradient, continues with a concave form for another ~20 km, ending a large knickpoint at Yancey Mill (Y) where there is an abrupt drop in channel elevation of ~3 m. This reach traverses the Chopawamsic Formation and Quantico Formation and is interrupted by small knickpoint at Horseshoe Farm. The epicentral region of the Mineral earthquake coincides with the Yancey Mill knickpoint, but the motion of the main rupture, had it

actually propagated to the surface as a single fault plane, is opposite in sense to what would be expected for generating that knickpoint. Downstream of Yancey Mill, the profile is linear or gently convex traversing mostly the Goochland terrane, interrupted by small knickpoints for another ~75 km, giving way to the large convexity at the Fall Zone where the channel falls 50 m in 45 km. The South Anna channel alternates between mostly alluvial reaches where bedrock is not present in the channel or along its banks, and bedrock reaches where bedrock and saprolite is exposed in the channel, along the banks, and in the hillslopes that form the valley wall. Except for the above mentioned prominent knickpoints, the bedrock reaches have gradients similar to the alluvial reaches. Furthermore, the knickpoints do not coincide with mapped geologic contacts or faults.

5.1.1 Channel steepness and steady-state elevations

Channel steepness (ks) of the South Anna River ranges from ~1 to 55 $m^{0.9}$ with the higher values located in the lower 45 km of the profile where the channel traverses the Fall Zone (**Fig. 5**). Excluding the knickpoints, a trend line passed through the k_{sn} values calculated from channel linear inversion shows that steepness gently rises from channel distance 90 km, is a maximum across the epicentral area, and gently falls upstream across the study reach. There are no obvious changes in channel steepness as the channel crosses mapped faults or lithologic boundaries.

A projection of the concave reach of the South Anna River above elevations of 135 m downstream across the lower, more convex reach intersects the ~12 Ma shallow marine Choptank Formation at an elevation of ~100 m (Weems et al., 2012; Edwards et al., 2018; **Fig. 5**). Correspondingly, river incision into the Virginia Piedmont at the Fall Zone by the South Anna and other rivers since the late middle Miocene is ~10 m/Myr as a long term average (Pavich et al., 1985; Pazzaglia, 1993), but can be as rapid as ~250 m/Myr (Reusser et al., 2004; 2006) where it is measured at prominent knickpoints and over shorter time spans. For comparison, along the James River in the western Piedmont, terrace deposits ~60 m to 75 m above the modern river channel have been cosmogenic-dated to ~1.1 Ma to 1.3 Ma (Hancock and Harbor, 2002; Hancock et al., 2004), indicating incision rates of ~45m/Myr.

The response time prediction (τ, eq. 4) of the South Anna channel to downstream base level fall compares well to the downstream projection shown in **Figure 5**. For these calculations, K values that range from 1.3×10^{-6} to 1.08×10^{-6} $yr^{-0.1}$ are used corresponding to the minimum and maximum k_{sn} values, respectively. Where the channel is 135 m in elevation, the predicted response time ranges from 10.5 to 12.5 Myrs, similar to the biostratigraphic age of the Choptank Formation. As described below, having a response time curve calibrated to the South Anna's representative concavity, steepness, and erosion rate is an important first step in being able to compare the modern South Anna valley bottom to paleovalley bottoms (terraces) as a means of quantifying crustal deformation.

The predicted steady-state elevation of the South Anna trunk channel using equation (5) closely follows the actual channel for ~10 km in the headwaters, but then rises above the channel

down to the Yancey Mill knickpoint, and then continues below the channel to the Coastal Plain (**Fig. 5**). This means that South Anna trunk channel flows higher than the steady-state prediction downstream of the epicentral region whereas the channel flows lower than the steady-state prediction upstream of the epicentral region.

Regionally, the South Anna River basin stands higher (**Fig. 5b**), and has higher chi (χ) values, on average (**Fig. 5c**), with respect to the North Anna drainage to the northeast and the James River to the southwest. Topographic swath profiles aligned with the South Anna River show a gentle, asymmetric rise in mean elevation above the earthquake epicentral region (**Fig. 5b**). Similarly, a map of stream channel steepness (k_{sn}) shows several particularly steep reaches (k_{sn} >50), including the knickpoints at Yancey Mill and Byrd Mill **(Fig. 5d)**. A similar steep reach on the North Anna River is not viewed as significant because it is at the outlet of the Lake Anna Reservoir and therefore is most likely an artefact of the DEM processing. Other high steepness reaches are present along the James River at tributary junctions where the lower reaches of the tributaries are steepened by the more deeply incised main James River channel.

5.1.2 Terrace geomorphic markers

Alluvial deposits between the towns of South Anna (Rt 522 bridge) and Byrd Mill (Rt 649 bridge) and another further upstream at the Virginia Vermiculite Mine (Rt. 22 west of Trevillians) provide the basis for terrace maps, geochronology, and stratigraphic models upstream and downstream of the 2011 earthquake (Malenda, 2015; Malenda et al., 2014; McGavick, 2017; **Fig. 6**). These alluvial deposits include those in the modern river valley bottom that continues to be reshaped by floods, as well as former valley bottoms that are perched between ~2 and ~40 m above the active floodplain where they mantle topographic flats and commonly underlie terrace landforms.

Six distinct allostratigraphic terraces that are the remnants of subparallel paleovalleys of the South Anna River are mapped and projected to the valley long profile (**Fig. 6**). These terraces are distinguished primarily on textural and relative weathering, and secondarily on elevation criteria. A mappable terrace unit consists of two or more inset deposits with treads at variable elevations, but straths (basal unconformities) that tend to cluster within 1-3 m for a given stream reach. The poor exposures and preservation of the deposits that underlie terraces Qt1, Qt2, and Qt3 introduce uncertainty in precisely locating the strath and identifying multiple alluvial units. However, for the younger terraces, the basal straths, critical for calculating incision rates, are well exposed. In addition, the fine exposures and preservation of terrace Qt4 show that it is composed of at least two deposits that are texturally distinct, exhibit different weathering characteristics, and have clear inset stratigraphic relationships. As a result, Qt4 is separated into an older Qt4a and younger, inset Qt4b map units.

Ages for the terraces shown in **Figure 6** are obtained from 30 luminescence samples that we have the most confidence in being derived directly from *in situ* terrace alluvium, complemented by stratigraphically bracketing colluvium and eolian deposits, and one TCN depth profile in

terrace Qt3. The details of all luminescence and TCN dating are presented in Pazzaglia et al., (in press).

5.1.3. TCN erosion rates

The mean TCN erosion rate calculated from seven alluvial samples throughout the South Anna catchment is 21.5±1.3 m/Myr, resulting from an average ^{10}Be concentration of 5.33x105 atoms/g. The highest erosion rates are calculated for samples collected in the epicentral region of the 2011 Mineral earthquake and the lowest rates are derived from the headwaters of the catchment where there is a low relief upland. The mean erosion rate is skewed by two rapid-rate samples within the epicentral region that may be influenced by local channel incision and contribution of low-concentration material to the alluvium. In contrast, the farthest downstream, basin-wide integrative South Anna River sample has a rate of 8.5±0.8 m/Myr, similar to the long-term rate of river incision at the Fall Zone. All TCN erosion rate data for the South Anna have been previously reported in USGS EHP Technical report G15AP00092 (Pazzaglia, 2107) and in Pazzaglia et al., (in press).

5.2 RLSZ – Pennsylvania Piedmont

Data taken from field studies of Tucquan Creek and Otter Creek show that (1) Tucquan Creek is systematically steeper than Otter Creek (**Fig. 7**), (2) there are prominent bedrock knickpoints at roughly, but not the same elevation in both streams (**Fig. 7**), (3) there is little variation in bedrock strength throughout the study area (**Fig. 8**), (4) bedrock is weakest in the active channel (**Fig. 8**), and (5) stream reaches trending parallel to the primary foliation strike direction (202°) have lower mean gradients than those flowing orthogonal to the foliation strike (**Figs. 9, 10, 11**).

5.2.1. Long profiles, knickpoints, and k_{sn} of trunk channels

Otter Creek and Tucquan Creek longitudinal profiles and in-field analysis confirm the presence of knickpoints at similar elevations, labeled 1 through 5. These knickpoints are associated with areas of increased channel steepness **(Fig. 7)**. Some Peaks in k_{sn} are unassociated with any knickpoints visible in the field and may represent discrepancies in the DEM, particularly where it has been corrected for infrastructure such as bridges. The spatial distribution of the knickpoints shown in long profile on **Figure 7** are visible as the warmer colors on the maps of **Figure 4b**. Using a reference channel concavity of 0.45, the mean catchment-wide channel steepness for Tucquan and Otter creeks is **23.1 m$^{0.9}$** and **14.7 m$^{0.9}$**, respectively.

5.2.2 Bedrock Structure and Strength

There is a wide range of bedrock compressive strength and rebound values (RV) along both the Otter Creek and Tucquan Creek trunk channels (**Fig. 8; Appendix A**). Mean RV for joints is

34 in Tucquan Creek and 35 in Otter Creek. In general, the bedrock compressive strength registers as harder, more elastic in the lower, incised reaches of both streams, particularly outside of the active channel where the rock is mostly dry. In the channel and particularly in the upstream, upland reaches of these streams, the compressive strength is relatively lower (**Fig. 8**). These broad patterns in field-measured compressive strength are broadly mirrored in the channel steepness (**Figs. 4b and 7**).

The dominant foliation is sub-horizontal striking 202 (**Fig. 9**). Mean RV for F1 foliation faces is very similar at 30 in Tucquan Creek and 31 in Otter Creek. The greatest measurement of compressive strength ($RV=54 \pm 35$) was taken in Tucquan Creek at 94 m, 10 m below the Erb Mill knickpoint (**Fig. 7, circled as knickpoint 2**). Joints are subvertical with preferred NNE (15º) and NW (305º) orientations (**Fig. 9**). Joint face RV is lowest in stream channels where the bedrock is exposed to intermittent wetting.

5.2.3   Stream Orientation with respect to structure

The planimetric paths of the Tucquan and Otter creek channels follow an obvious rectilinear path (**Fig. 4b**) suggestive of control by the joints and/or foliations. There is a weak coincidence between channel gradient and stream orientation as measured by the RLI (**Fig. 10**). In Tucquan Creek, where the trunk channel must flow towards the SW to reach the Susquehanna River (Fig. 4b), the dominate RLI is subparallel to the foliation, and orthogonal to the joints (**Fig. 10b**). In contrast, for Otter Creek that has to flow to the SE to reach the Susquehanna River, there are many channels that flow subparallel to the joins, and orthogonal to the foliation (**Fig. 10a**). The lowest channel steepness values for both streams is oriented SW-NE, specifically between 030-060 whereas the highest k_{sn} values are orthogonal to the foliation (**Fig. 11**). These DEM-based measurements coincide with the qualitative field observation that the channels are mostly devoid of any alluvium, and bedrock plucking is evident in the reaches that are orthogonal to the foliation. Collectively, for the whole catchment, these subtle variations in reach-length k_{sn} average out, and are superseded by the systematic increase in k_{sn} as the trunk channels approach the Susquehanna River (**Figs. 4b and 7**).

5.2.4. TCN erosion rates

Spatially averaged basin-wide erosion rates derived from TCN dating of alluvial samples (**Fig. 8a**) in this study yields an erosion rates that range from 9.0±0.8 m/Myr (OTT-3) to 15.0±1.3 m/Myr (OTT-7; **Table 1, Appendix B**). These extremes are both located in the Otter Creek basin and illustrate the seemingly random correlation among erosion rate, landscape position, and proximity to a channel knickpoint. OTT-3 was sampled from a steep tributary to the trunk channel in the deeply-incised reach where channel steepness is high whereas OTT-7 was sampled in an upland where channel steepness is low. Similarly, the mean erosion rate for the Otter Creek catchment, which has a lower mean steepness than Tucquan Creek, is 11.8±0.4

m/Myr in comparison to the lower mean catchment erosion rate for Tucquan Creek of 11.0±0.4 m/Myr.

Collectively, these tightly clustered erosion rate measurements average to 11.4±0.3 m/Myr and are not correlated to channel steepness (**Fig. 12**). This disconnect from channel steepness is an indication of significant transience in these catchments where the hillslopes and soil production rates have not yet come into balance with channel incision rates. These observations are completely consistent with the contrast between the narrow, incised river valleys, particularly close to the Susquehanna River, and the gently rolling, saprolite and soil mantled uplands. Mean Piedmont rock erodibility (K) considering both catchments is calculated from eq. (3) using the TCN erosion rate and the mean upstream k_{sn} at each TCN sample location with the assumption n=1, as **$9.7x10^{-7}$ m$^{0.1}$s^{-1}** (**Fig. 12**).

5.2.5 Exploration of K and n for Piedmont channels.

Channel steepness (k_{sn}) has been shown to co-vary with erosion rate (E), a proxy for rock uplift (U) in many tectonically active settings where these variables have a large range (Kirby and Whipple, 2012; Lague, 2013). Unfortunately for the Appalachians, and Pennsylvania Piedmont, there is a tight clustering of k_{sn} and E measurements making regression impractical (**Fig. 12**). Attempts at such regressions suggest that the power exponent on slope, n, in the stream power law (eqs. 1 and 3) may be 2 or greater. A n exponent > 1 means that the channel erosion process deviates from a pure detachment limited plucking mechanism and includes other processes, such as abrasion. Direct observation of channel bed erosion in Otter and Tucquan creeks strongly support detachment-limited plucking. There is a dearth of sediment to serve as abrasive tools, and the pervasive foliation and jointing renders the bedrock susceptible to plucking. The analysis proceeds on the assumption that n = 1 in this case, which allows us to force a regression line with that slope through our data (**Fig. 12**). The resulting regressions indicate rock erodibility (K) values similar in magnitude to those reported from other studies (Miller et al., 2013). Mean catchment-wide rock erodibilities (K) for Tucquan and Otter creeks of **$4.18x10^{-7}$m$^{0.1}$s^{-1} and $7.4x10^{-7}$m$^{0.1}$s^{-1}** are calculated from eq. 3 assuming a channel reference concavity of 0.45, an n=1, the mean, catchment wide channel steepness, and the measured TCN erosion rates respectively. Note that these values are similar to, but smaller (less erodible) than the **$9.7x10^{-7}$m$^{0.1}$s^{-1}** value calculated as a two-catchment mean.

5.2.6 Tucquan and Otter trunk channel response times and knickpoint elevation

Rock erodibility values are used in eq. 4 to calculate the trunk channel response times to base level fall. For this exercise, and in an effort to account for local rock erodibility, the mean catchment-wide rock erodibility values are used. The response time curves are plotted with respect to channel distance and shown as the gray curves on **Figure 13**. Where the response time curve intersects the channel distance location of a transient knickpoint, the response time, or the time since that knickpoint has propagated from the point of base level fall to its current location

is determined. In this argument, base level fall is taken to be impulsive and occurring at the Susquehanna River synchronously for the mouths of Tucquan and Otter creeks. This type of base level fall further mimics uniform block rock uplift in the Piedmont, the prediction of which states that knickpoints of similar age resulting from the same base level fall will move as a kinematic wave through the catchments and should be at similar elevations throughout (**Fig. 2**).

Using the Tucquan Creek response time curve as the reference, the ages of five transient knickpoints is shown to be 0.8, 3.1, 5.9, 9.5, and 15.4 Ma. These ages correspond to geomorphic and stratigraphic markers in the lower Susquehanna River valley and upland gravels on the Inner Coastal Plain (Pazzaglia, 1993; Pazzaglia and Gardner, 1993,) so the assumption of impulsive base level fall is a good first approximation. Again using the Tucquan Creek response time curve as the reference, predictions are made for where a same-aged knickpoint should be on Otter Creek. Intersection of the horizontal knickpoint age lines with the Otter Creek response time curve shows a mis-match in predicted knickpoint elevation. Particularly for knickpoints 1, 3, and 4, the knickpoints on Otter and lower, by up to 10 m, than their correspondingly aged knickpoints on Tucquan Creek (**Fig. 13**). This argues for non-uniform rock uplift, with Tucquan Creek experiencing more rock uplift over the past 15 Ma than Otter Creek.

5.2.7. Tucquan and Otter trunk channel predicted steady state elevation

The predicted steady-state channel elevations, using the catchment-wide channel steepness, are shown as the green curves on **Figure 13**.   These curves closely mirror the actual channel elevations because they have been constructed using the locally-calibrated stream steepness. But in both cases, the predicted channel elevation falls beneath the actual channel elevation, suggesting that channel steepness is transient, and not fully adjusted to the rate of base level fall. This disconnect between uplift (base level fall) and channel steepness is consistent with the lack of any co-variance between erosion rate and channel steepness. Predicted steady-state channel elevations that plot beneath the actual channel elevation suggests an acceleration of rock uplift (base level fall) over the past 15 Ma. This acceleration in rock uplift has led to steeper channels in Lancaster County with respect to York County.

5.2.8. Inversion of Tucquan and Otter creek channels for base level history

The history of base level fall is reconstructed using eqs 6 and 7, following the Goren et al., (2014) and Gallen (2018) channel linear inversion model (**Fig. 14**). When the local catchment erosion rate and channel steepness is considered, the model can delicately adjust for rock erodibility at the channel reach scale (**Fig. 14a**). The result are sub-parallel base level fall histories for Tucquan and Otter creeks that have three components: (1) an early, pre-10 Ma history of slow rock uplift of about 5 m/Myr, an acceleration of rock uplift between 10 and 1 Ma to rates of ~10-15 m/Ma, and a recent post-1 Ma spike in uplift at rates approaching 25-30 m/Ma.   These results are consistent with the plots of the steady-state channel elevations with respect to the actual channel elevations (**Fig. 13**).

In contrast, considering a mean, constant erosion rate of 11.4 m/Ma and a uniform channel steepness of 18.9 $m^{0.9}$ which is the mean of both catchments, assumes a uniform rock erodibility (K) of $6x10^{-7}$ $m^{0.1}s^{-1}$. This K value is similar to the other K values, calculated under different k_{sn} and E assumptions, described above in this report. The precise K value for this model analysis is not critical, all that is important is that it is assumed to be uniform which means that the base level fall history will be sensitive to non-uniform uplift. In this case, the same three part change in uplift history is evident, the rates are faster, and more importantly, Tucquan Creek plots systematically higher than Otter Creek (**Fig. 14b**). This argues for faster rock uplift beneath the Tucquan Creek catchment, consistent with its overall higher actual k_{sn} value. The effect of choosing a mean k_{sn} and constant K value in this model has the effect of underestimating the true amount of rock uplift beneath Tucquan, and overestimating the true amount of rock uplift beneath Otter, resulting in the divergent rock uplift histories.

5.2.9 Regional analysis of Piedmont channel predicted steady state elevation

Non-uniform rock uplift and crustal strains are explored by applying different parameterizations of eq. (5) with a $n=1$ and $\theta_{ref} = 0.45$ across eight adjacent catchments in York County including Otter Creek, and five adjacent watersheds in Lancaster County including Tucquan Creek (**Fig. 4; Appendix C**). All of these catchments, with the exception of L1, Pequea Creek, drain very similar metamorphic rock types of the High Piedmont (**Figs. 4, 15, 16, 17**). In contrast, Pequea Creek mostly drains clastic and carbonate rocks of the Low Piedmont (**Figs. 4, 15, 16, 17**) that almost certainly have a higher erodibility than the High Piedmont rocks. In all subsequent figures, the difference between the actual channel elevation and the predicted elevation is shown as cool-colored negative to warm-colored positive values (**Figs. 15, 16, 17**). The warm colors indicate where the actual channel elevation is higher than the predicted channel. The magnitude of the predicted difference in channel elevation is not as important as the general patterns that emerge. The Martic line, Tucquan antiform, Westminster anticline, and 1983 Lancaster earthquake are included as reference geologic, structural, geomorphic, and seismic observations.

5.2.9.1 Model 1. Piedmont-wide uniform k_{sn} of 14.8 $m^{0.9}$

This model assumes a constant k_{sn} value for all watersheds resulting from a simple average of the median k_{sn} for each of the 13 Piedmont catchments. Assuming a Piedmont-wide uniform k_{sn} means that in many places, this value is locally too low because either the rocks are hard (the K term in eq. 3), or the uplift is relatively fast (the U term in eq. 3). In other places, the k_{sn} value is locally too high because the rocks are soft or the uplift is relatively slow. The result is a model prediction that places the streams too low where the rocks are hard or uplift is fast, and too high where the rocks are soft and uplift is slow (**Fig. 15**). Discerning whether the resulting channel difference pattern is being driven by non-uniform erodibility or uplift requires some regional knowledge of the geology, structure, geomorphology, and seismic characteristics. In this case, the

emergent pattern of red channels mostly follows a NE-SW oriented bulls-eye pattern, centered on the Tucquan structural and Westminster topographic anticlines. Changes in rock-type (K) for the Pequea catchment (L1) in particular, likely also contribute to the overall pattern of predicted difference in channel elevation.

5.2.9.2 Model 2. Non-uniform, mean catchment k_{sn}.

Model 2 takes a step forward in trying to better account for local adjustments of k_{sn} to both erodibility (rock-type) and uplift at the catchment scale. The mean k_{sn} for each catchment is calculated from the DEM by summing and averaging all k_{sn} values at channel reach lengths of 1000 m using eq. (2). The resulting pattern of channels that are higher than model predictions (colored red) is different than the predictions of Model 1 (**Fig. 16**). In this case, Model 2 predicts that the north-draining tributaries of Pequea Creek that lie on the metamorphic rocks of the High Piedmont are much higher than the model prediction, whereas the rest of the Pequea channels are below model predictions, mimicking the distribution of the hard rocks of the High Piedmont with respect to the softer rocks of the Low Piedmont. Similarly, the predicted elevations of the channels of Tucquan and Otter creeks are close to their actual elevations, whereas those of Muddy Creek (Y8) are mostly higher than prediction. This is not a surprise as the k_{sn} of 11.8 m$^{0.9}$ was calibrated locally for Otter and Tucquan creeks. Farther away from this calibration, changes in erodibility and/or uplift will emerge as a mismatch in the model predictions. Based on the emergent pattern of red streams in Model 2, it seems that its predictions are most sensitive to rock-type and changes in K, and by extension k_{sn}.

5.2.9.3. Model 3. Non-uniform, reach-scale k_{sn}.

Model 3 goes one step further in predicting steady state channel elevations from local k_{sn}, adjustments to K and U by dividing channel reaches into 10-m elevation bins via a k_{sn} inversion technique (Gallen, 2018). At this scale, a steady-state channel should be delicately adjusted to all local variations in rock type (K) and uplift (U) and the predicted channel elevation should closely match the actual channel elevation. Of the three models, Model 3 should be most sensitive to transient channels that are not in steady-state. Two patterns emerge from the Model 3 predictions (**Fig. 17**). First, all of the predicted channel elevations are above actual channel elevations. All of the channel colors on the Model 3 map are negative, with the red colors indicating model elevations that are closest to actual elevations, but still higher. Second, the warmest colors are along the Susquehanna River, and the colors become progressively cooler further away. This pattern is consistent with transient waves of base level fall moving up through the catchments. The catchments and reaches closest to the base level fall have channel steepnesses (k_{sn}) most closely adjusted to the base level fall whereas the channels further away are progressively farther from the steady state condition suggested by the integrated distribution of k_{sn} from the mouth to headwaters of the channel. Non-uniform uplift is evident in Model 3, but it is the result

of non-steady incision of the Susquehanna River at the regional scale. Model 3 losses some resolution to discern non-uniform uplift among catchments like Model 2, but it also is almost completely insensitive to small variations in *K* that plague Model 2.

6. Interpretations

6.1. Introduction

This research aspires to use geomorphic markers and river long profiles to identify crustal strains, essentially acting as paleogeodetic indicators, in the slowly-deforming plate interior where the signal to noise ratio is low for both GPS and geologic geodesy. In the intraplate setting, crustal strains are ultimately derived from stresses that may be local, resulting from non-uniform vertical loads such as topographic (Levandowski et al., 2017), the GIA (Sella et al., 2007), or transient fluvial erosion (Gallen and Thigpen, 2018). Alternatively, they are regional derived from the focusing of plate tectonic stresses due to a fully-coupled, dynamic lithosphere-asthenosphere (Ghosh et al., 2019). In either case, the goal is to identify non-uniform rock uplift that indicates permanent strain resulting from persistent, long-term slip of active faults, or transient strain resulting from faults that might be locked over long, geologic timescales, but still seismogenic. The results presented above have taken a positive step forward in addressing these issues.

6.2 Strain in the CVSZ and earthquake recurrence intervals

Permanent crustal deformation primarily documented by the South Anna terraces and secondarily supported by the distribution of channel steepness and steady-state elevation shows that crustal deformation in the CVSZ is co-located with the non-uniform focusing of stresses in ENAM predicted by the coupled plate tectonic model (Ghosh et al., 2019). Mapping, dating, and correlation of river terraces along the South Anna River, that traverses the epicenter of the 2011 Mineral, VA intraplate earthquake, reveals a crustal deformation pattern consistent with the earthquake's location and sense of rupture even though neither the fault plane nor the rupture propagate to the surface (**Fig. 6**). Growth of an asymmetric crustal anticline, indicated by the rate of fluvial incision through these terraces, has a long-term average of ~20-30 m/Ma but is also unsteady, with a possible, particularly rapid period of growth occurring in the last ~200 kyrs at rates three times as rapid. The geomorphic marker data are further supported by river channel metrics and models including channel steepness (k_{sn}), chi (χ), response time (τ), and predicted steady-state channel elevation (**Fig. 5**).

Modeled coseismic deformation of the Mineral earthquake (Walsh et al., 2015) can be used with the terrace paleogeodetic data to estimate a recurrence interval of ~5.5 kyrs for Mineral-size earthquakes, assuming that only a single fault is driving the deformation. Considering that

seismological estimates of the recurrence interval of a Mineral-sized earthquake is an order of magnitude shorter for the CVSZ (Chapman et al., 2015) and that there was a large stress drop on the fault that ruptured in 2011 (Wu and Chapman, 2017), it is likely that more than one fault contributed to the observed crustal deformation. In any event, using geomorphic markers such as river terraces as paleogeodetic measures of crustal deformation can work in intraplate settings as a means of documenting tectonic processes and rates and in estimating seismic hazards.   This study purposely focused on a region where the location of the tectonic forcing was known from the 2011 Mineral earthquake, and predicted by an emerging class of coupled plate tectonic geodynamic models (Ghosh et al., 2019). It conceptually illustrates how geomorphic markers could be used to identify crustal deformation and potential seismic hazards for intraplate regions where faults may be locked, and there is no historical record of seismic activity.

6.3 Strain in the Pennsylvania Piedmont and relation to the 1983 Lancaster earthquake-causative fault.

Erosion rates, knickpoint elevations, reconstruction of base level fall (uplift) history, and modeling of the steady state channel elevation collectively point to non-uniform uplift in the Pennsylvania Piedmont proximal to the suspected causative fault that ruptured in the 1983 Mw 4.2 Lancaster earthquake. As in the CVSZ, geomorphic markers are proven to be effective measures of crustal strains in the slowly-deforming intraplate setting of the Pennsylvania Piedmont.

The Piedmont deformation is embedded in a more regional epeirogenic uplift of the entire mid-Atlantic margin (Rowley et al., 2013; Moodie et al., 2017), that is driving base level fall for the major Atlantic slope streams, such as the Susquehanna River and its tributaries, the catchments studied in this research. This regional uplift is accelerating, as suggested by modeling stream profiles using a uniform block-uplift, linear inversion approach (Goren et al., 2014; **Fig. 14**). As a result, there is a significant amount of transience in the geomorphic system expressed as channels where stream steepness (k_{sn}) is not fully adjusted and in steady-state with the rock uplift rate or rock-type (K). Furthermore, the hillslopes are not eroding as rapidly as the channels are incision resulting in catchment-averaged erosion rates that are more reflective of soil production rates in the uplands, rather than fluvial incision in the valleys. The transience is most evident in the modeling of the steady state elevation of river channels when stream steepness is calculated in 10-m elevation bins (**Fig. 17**). Such local calibration of k_{sn} values controls for non-uniform rock erodibility and uplift rate.

However, crustal strains emerge from the transient incision background as non-uniform uplift when rock erodibility is taken to be uniform and constant, a reasonable assumption given the field measurement of structural (**Figs. 9, 10**), channel orientation (**Fig. 11**), and uniformity schmidt-hammer rebound values (**Fig. 8**). Identification of transient knickpoints on the trunk channels of Tucquan Creek, which is proximal to the location of the 1983 Lancaster earthquake and RLSZ in Lancaster County, and Otter Creek, which is distal to the earthquake and lacks

RLSZ seismicity have climbed to different elevations in their respective catchments based on the channel response times (**Fig. 13**). Knickpoints of the same age are ~2-10 m higher in Tucquan Creek compared to Otter Creek. Similarly, the base level fall history for Tucquan Creek indicates more rapid rock uplift in comparison to Otter Creek, when a common, mean stream steepness is used (**Fig. 14b**).

The non-uniform uplift pattern in the Pennsylvania Piedmont is revealed as an elongated bulls-eye pattern centered on the mouth of Tucquan Creek and subparallel to the Tucquan structural and Westminster topographic antiforms (**Fig. 15**). The upwarp plunges towards the northeast into the Martic Line at the location of rift-related igneous dikes that have the same orientation of the suspected, but blind fault that ruptured in 1983 (**Fig. 15**). The upwarp is also coincident with the most narrow, deepest part of the Susquehanna River carved Piedmont gorge and an offset in upland gravel terraces (Pazzaglia and Gardner, 1993).

7. Conclusions and Recommendations

These studies in the RLSZ and CVSZ focused specifically on regions of known historic seismicity, where a number of geomorphic markers such as river terraces and transient knickpoints could be directly compared to catchment-wide erosion rates, channel response times, and the predicted elevation of steady-state channel profiles to document non-uniform rock uplift. The results help close the two critical knowledge gaps particularly acute in plate interiors: (1) lack of evidence of long-term time series of fault slip and (2) known locations of locked seismogenic faults with no historic slip history. For the former, this study shows that the crust has been deformed, and there is a topographic and geomorphic record of non-uniform rock and surface uplift in both the CVSZ and RLSZ. Such non-uniform uplift is a manifestation of the local stresses responsible for earthquakes. Given the slow strain rates, the interseismic period could be very long, resulting with many locked, but seismogenic faults hiding in plain site. This research shows that repeated fault slip will generate a crustal deformation signal that is measurable by geologic geodesy and the approaches detailed herein.

For knowledge gap (2), importantly, these approaches are portable to settings outside of seismic zones in CEUS that share a common base level. Settings with more uniform rock type simplify the interpretations of the data generated by these methods in terms of rock uplift and are capable of identifying locations of active, but locked faults. Studies could be constructed to choose random parts of the Appalachian Piedmont traversed by a major Atlantic Slope river, that lie in the seismic gaps between major seismic zones. The Maryland Piedmont traversed by the Potomac River is an obvious potential target for this analysis that would be specifically aimed at discerning crustal strains in the absence of historic seismicity.

8. Acknowledgment of Support and Disclaimer

9. References

Aragon, J. C.; Long, M. D.; and Benoit; M. H. 2017. Lateral variations in SKS splitting across the MAGIC array, central Appalachians. Geochemistry, Geophysics, Geosystems. 18. *https://doi.org/10.1002/2017GC007169*.

Argus, D. F.; and Peltier, W. R. 2010. Constraining models of postglacial rebound using space geodesy: a detailed assessment of model ICE-5G (VM2) and its relatives. Geophysical Journal International. 181(2): 697-723.

Armbruster, J. G. and Seeber, L., 1987, The 23 April 1984 Martic earthquake and the Lancaster seismic zone in eastern Pennsylvania: Bulletin of the Seismological Society of America, v. 77, no. 3, p. 877-890.

Balco, G., Stone, J. O., Lifton, N. A., and Dunai, T. J., 2008, A complete and easily accessible means of calculating surface exposure ages or erosion rates from 10Be and 26Al measuements: Quaternary Geology, 3, 174-195.

Baljinnyam, I.; Bayasgalan, A.; Borisov, B.; Cisternas, A.; Dem'yanovich, M. G.; Ganbaatar, L.; Kochetkov, V. M.; Kurushin, R. A.; Molnar, P.; Philip, H.; and Vashchilov, Y. Y. 1993. Ruptures of Major Earthquakes and Active Deformation in Mongolia and Its Surroundings. Geological Society of America Memoir 181: 62 p. 10.1130/MEM181-p1.

Berlin, M. M., and R. S. Anderson (2007), Modeling of knickpoint retreat on the Roan Plateau, western Colorado, J. Geophys. Res., 112, F03S06, doi:10.1029/2006JF000553.

Berti, C., Pazzaglia, F. J., Meltzer, A. S., and Harrison, R. W., 2015, Evidence for persistent, cumulative deformation of the Virginia Piedmont in the vicinity of the 23 August, 2011 Mineral earthquake, in Horton, J. W., Chapman, M. C., and Green, R. A., eds., The August 23, 2011 Earthquake in Central Virginia and its Significance for Seismic Hazards in Eastern North America: Geological Society of America Special Paper 509, p. 1-14, doi:10.1130/2015.2509(21).

Bierman, P. and Steig, E.J., 1996. Estimating rates of denudation using cosmogenic isotope abundances in sediment: Earth surface processes and landforms, 21(2), pp.125-139.

Biryol, C. B.; L. S. Wagner; K. M. Fischer; and R. B. Hawman 2016. Relationship between observed upper mantle structures and recent tectonic activity across the Southeastern United States. J. Geophys. Res. Solid Earth. 2015JB012698. doi:10.1002/2015JB012698.

Brooks, E. M., Neely, J., Stein, S., Spencer, B. D., Salditch, L., 2019, Assessments of the performance of the 2017 one-year seismic hazard forecast for the central and eastern United States via simulated earthquake shaking data: Seismological Research Letters, 90, 1155-1167.

Brown, N. D. 2020. Which geomorphic processes can be informed by luminescence measurements? Geomorphology. 367:107296.

Calais, E. and Stein, S. 2009. Time variable deformation in the New Madrid seismic zone.

Science. 323:1442.

Calais, E., Han, J.; DeMets, C.; and Nocquet, J. M. 2006. Deformation of the North American plate interior from a decade of continuous GPS measurements. J. Geophys. Res. 111: doi:10.1029/2005JB004253.

Campbell, M., 1929, Late geologic deformation of the Appalachian Piedmont as determined by river gravels: Proceedings of the National Academy of Sciences of the U.S., 15, 2, 156-161.

Chapman, M. C. 2013. On the rupture process of the 23 August 2011 Virginia Earthquake. Bulletin of Seismological Society of America. 103:613-628.

Chapman, M. C.; Beale, J. N.; Hardy, A. C.; and Wu, Q. 2016. Modern seismicity and the fault responsible for the 1886 Charleston, South Carolina earthquake. Bulletin of the Seismological Society of America. 106: 364-372.

Chapman, M.C., 2015, Magnitude, recurrence interval, and near-source ground-motion modeling of the Mineral, Virginia, earthquake of 23 August 2011, in Horton, J.W., Jr., Chapman, M.C., and Green, R.A., eds., The 2011 Mineral, Virginia, Earthquake, and Its Signifi cance for Seismic Hazards in Eastern North America: Geological Society of America Special Paper 509, p. 27–45, doi:10.1130/2015.2509(02).

Crosby, B. T., and K. X. Whipple (2006), Knickpoint initiation and distribution within fluvial networks: 236 waterfalls in the Waipaoa River, North Island, New Zealand, Geomorphology, 82, 16 – 38, doi:10.1016/ j.geomorph.2005.1008.1023.

Cyr, A.J., Granger, D.E., Olivetti, V. and Molin, P., 2010. Quantifying rock uplift rates using channel steepness and cosmogenic nuclide–determined erosion rates: Examples from northern and southern Ital:. Lithosphere, 2(3), pp.188-198.

DiBiase, R. A. 2018. Short communication: Increasing vertical attenuation length of cosmogenic nuclide production on steep slopes negates topographic shielding corrections for catchment erosion rates. Earth Surface Dynamics. 6:923-931.

Ebel, J. E. 2009. Analysis of aftershock and foreshock activity in stable continental regions; implications for aftershock forecasting and the hazard of strong earthquakes. Seismological Research Letters. 80:1062-1068.

Edwards, L. E.; Weems, R. E.; Carter, M. W.; Powars, D. S.; and Spears, D. B. 2018. The significance of dinoflagellates in the Miocene Choptank Formation beneath the Midlothian gravels in the southeastern Virginia Piedmont. Stratigraphy. 15: 179–195. doi:10.29041/strat.15.179-195.

Ellsworth, W. L., Imanishi, K; Luetgert, J. H.; and Hamilton, J. 2011. The Mw5.8 Virginia earthquake of August 23, 2011 and its aftershocks: A shallow high stress drop event. American Geophysical Union 44th annual Fall Meeting. Abstract S14B-05.

Flint, J. J. 1974. Stream gradient as a function of order, magnitude, and discharge. Water Resources Research. 10:969–973.

Freedman, J., Wise, D.U., Bentley, R.D., 1964, Pattern of Folded Folds in the Appalachian Piedmont Along Susquehanna River: GSA Bulletin, 75 (7), 621-638. Doi: https://doi.org/10.1130/0016-7606(1694)75[621:POFFIT]2.0.CO;2

Gallen, S. F. 2018. Lithologic controls on landscape dynamics and aquatic species evolution in post-orogenic mountains. Earth and Planetary Science Letters. 493:150-160.

Gallen, S. F. and Thigpen, J. R. 2018. Lithologic controls on focused erosion and intraplate earthquakes in the Eastern Tennessee Seismic Zone. Geophysical Research Letters. 45:9569-9578.

Ghosh, A.; Holt, W. E.; and Bahadori, A. 2019. Role of large-scale tectonic forces in intraplate earthquakes of central and eastern North America. Geochemistry, Geophysics, Geosystems. 20:2134–2156. *https://doi.org/10.1029/2018GC008060*.

Ghosh, A.; Holt, W. E.; and Wen, L. 2013. Predicting the lithospheric stress field and plate motions by joint modeling of lithosphere and mantle dynamics. Journal of Geophysical Research Solid Earth. 118:346-368.

Gonzales, J. M., 2019, Using knickpoints as geomorphic markers of crustal deformation in Appalachian Piedmont seismic clusters: MS Thesis, Bethlehem, PA, Lehigh University, 87 p.

Gordon, R. G. 1998. The plate tectonic approximation: Plate nonrigidity, diffuse plate boundaries, and global plate reconstructions. Annual Reviews of Earth and Planetary Sciences. 26:615-642.

Goren, L., Fox, M., and Willett, S. D., 2014, Tectonics from fluvial topography using formal linear inversion theory: Theiry and applications to the Inyo Mounntains, California: Journal of Geophysical Research Earth Surface, 119, 1651-1681.

Granger, D.E., Kirchner, J.W. and Finkel, R., 1996. Spatially averaged long-term erosion rates measured from in situ-produced cosmogenic nuclides in alluvial sediment: The Journal of Geology, pp.249-257.

Hack, J. T. 1957. Studies of longitudinal stream profiles in Virginia and Maryland. U.S. Geological Survey Professional Paper. 294-B:45-97.

Hancock, G. S. and Harbor, D. J. 2002. Cosmogenic isotope dating of rapid, disequilibrium incision of the James River in central Virginia. Geological Society of America Abstracts with Programs. 34:8.

Hancock, G. S.; Harbor, D. J.; Felis, J.; and Turcotte, J. 2004. [10]Be Dating Of River Terraces Reveals Piedmont Landscape Disequilibrium in the Central James River Basin, Virginia, SE Geological Society of America. GSA Abstracts with Programs. 36:2.

Harkins, N.; Kirby, E.; Heimsath, A.; Robinson, R.; and Reiser, U. 2007. Transient fluvial incision in the headwaters of the Yellow River, northeastern Tibet, China. Journal of Geophysical Research. Earth Surface. 112:F03S04. doi:10.1029/2006JF000570.

Herrmann, R. B. 2011. St. Louis University Earthquake Center website. http://www.eas.slu.edu/eqc/eqc_mt/MECH.NA/20110823175105/index.html

Hill, J. C., 2007, Bedrock geologic map of the northern portion of the Holtwood and Wakefield quadrangles, Lancaster and York Counties, Pennsylvania: PA Geological Survey Open File Report OFBM-07-04.0.

Horton, J. W. Jr. and Williams, R. 2012. The 2011 Virginia earthquake: What are scientists learning? EOS Transactions, American Geophysical Union. 93:317-318.

Horton, J. W. Jr.; Drake, A. A.; Jr., and Rankin, D. W. 1989. Tectonostratigraphic terranes and their Paleozoic boundaries in the Central and Southern Appalachians, *in* Dallmeyer, R.D., ed., Terranes in the Circum-Atlantic Paleozoic Orogens. Geological Society of America Special Paper. 230:213-245.

Horton, J. W. Jr.; Shah, A. K.; McNamara, D. E.; Snyder, S. L.; and Carter, A. M. 2015. Aftershocks illuminate the 2011 Mineral, Virginia, earthquake causative fault zone and nearby active faults, *in* Horton, J. W., Jr.; Chapman, M.C.; and Green, R.A. eds. The 2011 Mineral, Virginia, Earthquake, and Its Significance for Seismic Hazards in Eastern North America. Geological Society of America Special Paper. 509:253–271. doi:10.1130/2015.2509(14).

Howard, A. D. 1994. A detachment-limited model of drainage basin evolution. Water Resources Research. 30:2261–2285.

Howard, A. D. and Kerby, G. 1983. Channel changes in badlands, Geological Society of America Bulletin. 94:739–752.

Hughes, K. S.; Hibbard, J. P.; and Miller, B. V. 2013. Relationship between the Ellisville pluton and Chopawamsic fault: Establishment of significant Late Ordovician faulting in the Appalachian Piedmont of Virginia. American Journal of Science. 45:584-612.

Hulbert, C.; Rouet-Leduc, B.; Johnson, P. A.; Ren, C. X.; Riviere, J.; Bolton, D. C.; and Marone, C. 2019. Similarity of fast and slow earthquakes illuminated by machine learning. Nature Geoscience. 12:69-74. https://doi.org/10.1038/s41561-018-0272-8.

Jonas, A.I., Stose, G.W., 1930, Geology and mineral resources of the Lancaster Quadrangle, Pennsylvania: Atlas of Pennsylvania, n. 168, Pennsylvania Geologic Survery, p. 106, 4th series, Atlas 168, Harrisburg, PA.

King, T. R.; Quigley, M.; and Clark, D. 2019. Surface-rupturing historical earthquakes in Australia and their environmental effects: New insights from re-analyses of observational data. Geosciences. 9:408, *https://doi.org/10.3390/geosciences9100408*.

Kirby, E. and Whipple, K. X. 2001. Quantifying differential rock-uplift rates via stream profile analysis. Geology. 29:415-418.

Kirby, E. and Whipple, K. X. 2012. Expression of active tectonics in erosional landscapes. Journal of Structural Geology. 44:54–75.

Knopf, E.B., Jonas, A.I., 1929, Geology of the McCails Ferry- Quarryville district, Pennsylvania: U.S. Geologic Survey Bulletin, 799(1929), p. 156.

Lague, D. 2013. The stream power river incision model: evidence, theory and beyond. Earth

Surface Processes and Landforms. doi:10.1002/esp.3462.

Levandowski, W.; Zellman, M.; and Briggs, R. 2017. Gravitational body forces focus North American intraplate earthquakes. Nature Communications. doi:10.1038/ncomms14314.

Liu, M.; Stein, S.; and Wang, H. 2011. 2000 years of migrating earthquakes in North China: How earthquakes in midcontinents differ from those at plate boundaries. Lithosphere. doi: 10.1130/L129.1.

Long, M. D.; Benoit, M. H.; Aragon, J. C.; and King, S. D. 2019. Seismic imaging of mid-crustal structure beneath central and eastern North America: Possibly the elusive Grenville deformation. Geology. *https://doi.org/10.1130/G46077.1*.

Long, M. D.; Ford, H. A.; Abrahams, L.; and Wirth, E. A. 2017. The seismic signature of lithospheric deformation beneath eastern North America due to Grenville and Appalachian orogenesis. Lithosphere. 9:987-1001.

Malenda, H. F.; Raup, C.; Pazzaglia, F. J.; and Berti, C. 2014. Surficial Geologic Map of the South Anna River in the Ferncliff and Pendleton Quadrangles, Virginia. USGS EDMAP Open File Map G13AC0015. Scale 1:24,000.

Malenda, H. M. 2015. New Quaternary geochronometric constraints on river incision in the Virginia Piedmont: Relative contributions of climate, base level fall, knickpoint retreat, and active tectonics [MS Thesis]. Bethlehem, PA. Lehigh University. 82 p.

Marple, R. T., and P. Talwani, 2000, Evidence for a buried fault system in the Coastal Plain of the Carolinas and Virginia—Implications for neotectonics in the southeastern United States. Geological Society of America Bulletin 112 (2), 200–220.

Matmon, A., Bierman, P. R., Larsen, J., Southworth, S., Pavich, M. J., Caffee, M. W., 2003, Temporally and spatially uniform rates of erosion in the southern Appalachian Great Smoky Mountains: Geology, v. 31, p. 155-158.

McCaffrey, R. 2009. The tectonic framework of the Sumatran subduction zone. Annual Reviews of Earth and Planetary Science. 37:3.1-3.22.

McCalpin, J., ed., 2009, Paleoseismology, 2nd edition. International Geophysics Series 95. 629 p.

McGavick, M. T. 2017. Exogenic and autogenic terrace formation processes along the South Anna River, Virginia. M.S. Thesis. Lehigh University. 83 p.

McGavick, M. T. 2017. Exogenic and autogenic terrace formation processes along the South Anna River, Virginia. M.S. Thesis. Lehigh University. 83 p.

McKenzie D. and Parker R. L. 1967. The North Pacific: an example of tectonics on a sphere. Nature 216:1276–1280.

McNamara, D. E.; Benz, H. M.; Herrmann, R. B.; Bergman, E. A.; and Chapman, M. 2014a. The Mw 5.8 central Virginia seismic zone earthquake sequence of August 23, 2011: Constraints on earthquake source parameters and fault geometry. Seismological Society of America Bulletin. 104:40–54. doi:10.1785/0120130058.

McNamara, D. E.; Gee, L.; Benz, H.; and Chapman, M. 2014b. Frequency dependent seismic

attenuation in the eastern US as observed from the 2011 central Virginia earthquake and aftershock sequence. Seismological Society of America Bulletin. 104:55–72. doi:10.1785/0120130045.

Miller, S. Sak, P. B., Kirby, E., and Bierman, P. R., 2013, Neogene rejuvenation o central Appalachian topography: Evidence for differential rock uplift from stream profiles and erosion rates: Earth and Planetary Science Letters, 369-370, 1-12.

Moodie, A. J., Pazzaglia, F. J., and Berti, C., **2017**, Exogenic forcing and autogenic processes on continental divide location and mobility: Basin Research, 30, 344-369, doi: 10.1111/bre.12256.

Morgan WJ. 1968. Rises, trenches, great faults, and crustal blocks. J. Geophys. Res. 73:1959–1982.

Morisawa, M. E. 1962. Quantitative geomorphology of some watersheds in the Appalachian Plateau. Geological Society of America Bulletin. 73:1025-1046.

Moucha, R. and Ruetenik, G. A. 2017. Interplay between dynamic topography and flexure along the U.S. Atlantic passive margin: Insights from landscape evolution modeling. Global and Planetary Change. 149:72-78.

Muir-Wood, R. 2000. Deglaciation seismotectonics: A principal influence on intraplate seismogenesis at high latitudes. Quaternary Science Reviews. 19:1399-1411.

Murphy, B. P., Johnson, J. P. L., Gasparini, N. M., Hancock, G. S., and Small, E. E., 2018, Weathering and abrasion of bedrock stream topography: Geology, *https://doi.org/10.1130/G40186.1*.

Niemann, J. D., Gasparini, N. M., Tucker, G. E., and Bras, R. L., 2001, A quantitative evaluation of Playfair's Law and its use in testing long-term stream erosion models: Earth Surface Processes and Landforms, 26, 1317-1332.

Pavano, F., Pazzaglia, F. J., and Catalano, S., 2016, Knickpints as geomorphic markers of active tectonics: A case study from northeastern Sicily (southern Italy): Lithosphere, doi:10.1130/L577.1.

Pavich, M. J.; Brown, L.; Valette-Silver, J. N.; Klein, J.; and Middleton, R. 1985. [10]Be analysis of a Quaternary weathering profile in the Virginia Piedmont. Geology. 13:39-41.

Pavlides, L. 1989. Early composite mélange terrane, central Appalachian Piedmont, Virginia and Maryland; Its origin and tectonic history. Geological Society of America Special Paper. 228:135-193.

Pazzaglia, F. J. 1993. Stratigraphy, petrography, and correlation of late Cenozoic middle Atlantic Coastal Plain deposits: Implications for late-stage passive margin geologic evolution. Geol. Soc. of Am. Bull. 105:1617-1634.

Pazzaglia, F. J. and Gardner, T. W., 1993, Fluvial terraces of the lower Susquehanna River: Geomorphology, v.8, p.83-113.

Pazzaglia, F. J., 2017, USGS Award G15AP00092: Geomorphic expression of the seismotectonics and seismic potential of source zones in CEUS: CVSZ and Charleston.

Pazzaglia, F.J., Malenda, H.F., McGavick, M. L., Raup, C., Carter, M.W., Berti, C., Mahan, S., Nelson, M., Rittenour, T.M., Counts, R., Willenbring, J., Germanoski, D., Peters, S. C., and Holt, W.D., in press, River terrace evidence of tectonic processes in the eastern North American plate interior, South Anna River, Virginia: Journal of Geology, 000, 000-000.

Peltier, W. R.; Argus, D. F.; and Drummond, R. 2015. Space geodesy constrains ice-age terminal deglaciation: The global ICE-6G_C (VM5a) model. J. Geophys. Res. Solid Earth. 120:450-487. doi:10.1002/2014JB011176.

Perron, J. T. and Royden, L. 2013. An integral approach to bedrock river profile analysis. Earth Surface Processes and Landforms. 38:570–576.

Portenga, E. W., Bierman, P. R., Rizzo, D. M., and Rood, D. H., 2013, Low rates of bedrock erosion in the central Appalachian Mountains inferred from in situ [10]Be: Geological Society of America Bulletin, 125, 201-215.

Pritchard, M. E. and Yun, S.-H. 2015. Satellite radar imaging and its application to natural hazards, in Singh, R. and Bartlett, D., eds., Natural Hazards, Earthquakes, Volcanoes, and Landslides. Boca Raton, LA. CRC Press, 20 p.

Reid, H.F., 1910. The Mechanics of the Earthquake, the California Earthquake of April 18, 1906, Report of the State Investigation Commission 2. Carnegie Institution of Washington, Washington, D.C.

Reusser, L. J.; Bierman, P. R.; Pavich, M. J.; Zen, E.-A.; Larsen, J.; and Finkel, R. 2004. Rapid Late Pleistocene incision of Atlantic passive-margin river gorges. Science. 305:499-502.

Reusser, L.; Bierman, P.; Pavich, M.; Larsen, J.; and Finkel, R. 2006. An episode of rapid bedrock channel incision during the last glacial cycle, measured with 10Be. American Journal of Science. 306:69-102.

Rouet-Leduc, B.; Hulbert, C.; Lubbers, N.; Barros, K.; Humphreys, C. J.; and Johnson, P. A. 2017. Machine learning predicts laboratory earthquakes. Geophysical Research Letters. 44:9276–9282.

Rovere, A; Hearty, P. J.; Austermann, J; Mitrovica, J. X.; Gale, J.; Moucha, R.; Forte, A. M; and Raymo, M. E. 2015. Mid-Pliocene shorelines of the US Atlantic coastal plain - an improved elevation database with comparison to Earth model predictions. Earth Science Review. 145:117–131.

Rowley, D. B., Forte, A. M., Moucha, R., Mitrovica, J. X., Simmons, N. A., and Grand, S. P., 2013, Dynamic topography change of the eastern United States since 3 million years ago: Science, 340, 1560-1563.

Salditch, L., Stein, S., Neely, J., Spencer, B. D., Brooks, E. M., Agnon, A., and Liu, M., 2020, Earthquake supercycles and long-term fault memory: Tectonophysics, 774, https://doi.org/10.1016/j.tecto.2019.228289.

Schmandt, B. and F.-C. Lin 2014. P and S wave tomography of the mantle beneath the United States. Geophys. Res. Lett. 41:6342–6349. doi:10.1002/2014GL061231.

Schwanghart, W. and Scherler, D. 2014. TopoToolbox 2 – MATLAB-based software for topographic analysis and modeling in Earth surface sciences. Earth Surface Dynamics 2:1–7. doi: 10.5194/esurf-2-1-2014.

Sella, G. F.; Stein, S.; Dixon; T. Craymer, M.; James, T.; Mazzotti, S.; and Dokka, R. 2007. Observations of glacial isostatic adjustment in stable North America with GPS. Geophys. Res. Lett. 34:doi:10.1029/2006GL02708.

Sella, G. F.; Stein, S.; Dixon; T. Craymer, M.; James, T.; Mazzotti, S.; and Dokka, R. 2007. Observations of glacial isostatic adjustment in stable North America with GPS. Geophys. Res. Lett. 34:doi:10.1029/2006GL02708.

Shen, W. and Ritzwoller, M. H. 2016. Crustal and uppermost mantle structure beneath the United States. J. Geophys. Res. Solid Earth. 121:4306–4342. doi:10.1002/2016JB012887.

Shimazaki, K., Nakata, T., 1980. Time-predictable recurrence model of large earthquakes. Geophs. Res. Lett. 7, 279–282.

Shobe, C. M., Hancock, G. S., Eppes, M. C., and Small, E. E., 2017, Field evidence for the influence of weathering on rock erodibility and channel form in bedrock rivers: Earth Surface Processes and Landforms: 42, 1997-2012.

Snyder, N. P.; Whipple, K. X.; Tucker, G. E.; and Merritts, D. J. 2000. Landscape response to tectonic forcing: Digital elevation model analysis of stream profiles in the Mendocino triple junction region, northern California. Geological Society of America Bulletin. 112:1250-1263.

Soto-Cordero, L.; Meltzer, A.; and Stachnik, J. C. 2018. Crustal structure , intraplate seismicity, and seismic hazard in the mid-Atlantic United States. Seismological Research Letters. 89: 241-252.

Stein, S. and Liu, M. 2009. Long aftershock sequences within continents and implications for earthquake hazard assessment. Nature. 462:87-89.

Stein, S.; Geller, R.; and Liu, M. 2012. Why earthquake hazard maps often fail and what to do about it. Tectonophysics. 562-563:1-25.

Stockar, D. V., 1986, Contemporary tectonics of the Lancaster, Pennsylvania seismic zone: M.S. Thesis, The Pennsylvania State University, University Park, 226 p.

Subarya, C.; Chlieh, M.; Prawirodirdjo, L.; Avouac, J-P.; Bock, Y.; Sieh, K.; Meltner, A. J.; Natawidjaja, D. H.; and McCaffrey, R. 2006. Plate-boundary deformation associated with the great Sumatra-Andaman earthquake. Nature. 440:46-51.

Turcotte, D. L. and Schubert, G. 2014. Geodynamics, Third Edition. Cambridge. Cambridge University Press. 636 p.

Tuttle, M. P.; Schweig, E. S.; Sims, J. D.; Lafferty, R. H.; Wolf, L. W.; and Haynes, M. L. 2002.

The earthquake potential of the New Madrid seismic zone. Bulletin of the Seismological Society of America. 92:2080-2089.

Valentino, D.W. Peavy, S.T., Valentino, R.W., 2004, Alleghanian orogenic-float on the Martic thrust during dextral transpression, central Appalachian Piedmont: Journal of Geodynamics, V. 37, 3, 613-631.

Van Arsdale, R. B.; Cox, R. T.; and Lumsden, D. N. 2019. Quaternary uplift in the lower Mississippi River Valley. Journal of Geology. 127:1-13.

Wallace, R.E., 1987. Grouping and migration of surface faulting and variation in slip rates on faults in the Great Basin province. Bull. Seismol. Soc. Am. 77, 868–877.

Walsh, L. S.; Montesi, L. G. J.; and Martin, A. J. 2015. Coulomb stress transfer and modeled permanent vertical surface deformation from the August 2011, Mineral, Virginia, earthquake *in* Horton, J. W. Jr.; Chapman, M. C.; and Green, R. A., eds. The 2011 Mineral, Virginia, earthquake, and its significance for seismic hazards in eastern North America. Geological Society of America Special Paper. 509: doi:10.1130/2015.2509(18).

Weems, R. E.; Edwards, L. E.; Carter, M. W.; and Spears, D. B. 2012. Middle Miocene dinoflagellates demonstrate the presence of upper Choptank marine beds beneath the Midlothian gravels in southern Virginia. Geological Society of America Abstracts with Programs. 44:537.

Whipple, K. X. and Tucker, G. E. 1999. Dynamics of the stream power river incision model: Implications for height limits of mountain ranges, landscape response timescales and research needs. Journal of Geophysical Research. 104:17,661–17,674.

Whipple, K. X.; DiBiase, R. A.; and Crosby, B. T. 2013. Bedrock Rivers *in* Shroder, J. (Editor in Chief), Wohl, E. ed. Treatise on Geomorphology. Academic Press. San Diego, CA, Fluvial Geomorphology. 9:550–573.

Whipple, K. X.; Forte, A. M.; DiBiase, R. A.; Gasparini, N. M.; and Ouimet, W. B. 2017. Timescales of landscape response to divide migration and drainage capture: Implications for the role of divide mobility in landscape evolution. J. Geophys. Res. Earth Surf. 122: doi:10.1002/2016JF003973.

Willett, S. D.; Hovius, N.; Brandon, M. T.; and Fisher, D. 2006. Tectonics, climate, and landscape evolution. Geological Society of America Special Publication. 398:449 p.

Willett, S. D.; McCoy, S. W.; Perron, J. T.; Goren, L.; and Chen, C. Y. 2014. Dynamic reorganization of river basins. Science, 343:1248765. doi:10.1126/science.1248765.

Wolin, E.; Stein, S.; Pazzaglia, F. J.; Meltzer, A. S.; Kafka, A.; and Berti, C. 2012, Mineral, Virginia, earthquake illustrates seismicity of a passive-aggressive margin. Geophys. Res. Lett. 39:doi.10.1029/2011GL050310.

Wu, Q. and Chapman, M. C. 2017. Stress-drop estimates and source scaling of the 2011 Mineral, Virginia, mainshock and aftershocks. Bulletin of the Seismological Society of America. 107:

2703-2720.

Wu, Q.; Chapman, M. C.; and Beale, J. N. 2015. The aftershock sequence of the 2011 Mineral, Virginia, earthquake: Temporal and spatial distribution, focal mechanisms, regional stress, and the role of Coulomb stress transfer. Bull. Seismol. Soc. Am. 105:2521–2537.

Wu, Q.; Chapman, M. C.; and Beale, J. N. 2015. The aftershock sequence of the 2011 Mineral, Virginia, earthquake: Temporal and spatial distribution, focal mechanisms, regional stress, and the role of Coulomb stress transfer. Bull. Seismol. Soc. Am. 105:2521–2537.

Table 1. TCN erosion rates for Tucquan and Otter Creeks

Table 1: Erosion Rates

Sample Name	Latitude	Longitude	Elevation
OTT-1	39.87792	- 76.38585	55
OTT-3	39.88854	- 76.40287	105
OTT-4	39.8895	- 76.41692	115
OTT-5	39.88966	- 76.4176	115
OTT-6	39.89037	- 76.41823	112
OTT-7	39.90366	- 76.46751	160
OTT-8	39.91049	- 76.47721	170
TUC-1	39.85818	- 76.34832	55
TUC-2	39.86003	- 76.34119	78
TUC-3	39.86856	- 76.33908	115
TUC-4	39.86385	- 76.33786	107
TUC-5	39.8698	- 76.30392	163
TUC-6	39.87792	- 76.28753	206

Sample Name	Quartz Mass g	Mass of 9Be Added µg*	AMS Cathode Number
OTT-1	21.9185	250.3	151643
OTT-3	23.0931	250.1	151644
OTT-4	21.9522	249.4	151645
OTT-5	21.88	249.6	151646
OTT-6	19.981	251.4	154577
OTT-7	21.821	249.6	151647
OTT-8	20.0351	250.9	154578
TUC-1	21.9741	248.7	151649
TUC-2	21.9804	249.5	153400
TUC-3	17.2038	249.7	153401
TUC-4	21.9737	248.8	153402
TUC-5	22.0228	247.9	153403
TUC-6	19.9502	250.0	154579

Sample Name	Uncorrected 10Be/9Be Ratio**	Uncorrected 0Be/9Be Ratio Uncertainty*	Background-Corrected 10Be/9Be Ratio
OTT-1	4.51e-13	1.04e-14	4.47e-13
OTT-3	6.19e-13	1.51e-14	6.15e-13
OTT-4	5.28e-13	1.14e-14	5.24e-13
OTT-5	4.50e-13	1.07e-14	4.45e-13
OTT-6	3.89e-13	8.58e-15	3.85e-13
OTT-7	3.88e-13	8.76e-15	3.83e-13
OTT-8	4.48e-13	8.57e-15	4.44e-13
TUC-1	4.69e-13	1.04e-14	4.64e-13
TUC-2	4.66e-13	1.24e-14	4.61e-13
TUC-3	3.98e-13	1.08e-14	3.94e-13
TUC-4	4.41e-13	1.19e-14	4.37e-13
TUC-5	5.46e-13	1.28e-14	5.41e-13
TUC-6	5.35e-13	1.12e-14	5.31e-13

Table 1: Erosion Rates (cont.)

Sample Name	Background-Corrected 10Be/9Be Ratio Uncertainty	10Be Concentration atoms g-1	10Be Concentration Uncertainty (atoms g-1)
OTT-1	1.05e-14	3.41e+05	7.98e+03
OTT-3	1.51e-14	4.45e+05	1.09e+04
OTT-4	1.14e-14	3.98e+05	8.64e+03
OTT-5	1.07e-14	3.39e+05	8.18e+03
OTT-6	8.59e-15	3.24e+05	7.23e+03
OTT-7	8.78e-15	2.93e+05	6.71e+03
OTT-8	8.59e-15	3.72e+05	7.19e+03
TUC-1	1.04e-14	3.51e+05	7.86e+03
TUC-2	1.24e-14	3.50e+05	9.40e+03
TUC-3	1.09e-14	3.82e+05	1.05e+04
TUC-4	1.19e-14	3.31e+05	8.98e+03
TUC-5	1.29e-14	4.07e+05	9.66e+03
TUC-6	1.12e-14	4.45e+05	9.35e+03

Sample Name	Erosion Rate m/My	Internal Uncertainty m/Myr	External Uncertainty m/Myr
OTT-1	11.5	0.3	1.0
OTT-3	9.0	0.2	0.8
OTT-4	10.3	0.2	0.9
OTT-5	12.2	0.3	1.1
OTT-6	12.9	0.3	2.1
OTT-7	15.0	0.4	1.3
OTT-8	11.6	0.2	1.0
TUC-1	11.2	0.3	0.9
TUC-2	11.2	0.3	1.0
TUC-3	10.7	0.3	0.9
TUC-4	12.5	0.4	1.1
TUC-5	10.5	0.3	0.9
TUC-6	9.9	0.2	0.8

Sample Name	Calculated Values:	Upstream Average ksn m=0.45	Upstream Average K n=1
OTT-1		13.6	8.43e-07
OTT-3		17.5	5.14e-07
OTT-4		13.5	7.61e-07
OTT-5		14.4	8.45e-07
OTT-6		12.0	1.08e-06
OTT-7		9.3	1.61e-06
OTT-8		8.7	1.33e-06
TUC-1		19.7	5.68e-07
TUC-2		35.3	3.17e-07
TUC-3		18.3	5.86e-07
TUC-4		16.6	7.54e-07
TUC-5		16.2	6.50e-07
TUC-6		16.0	6.19e-07

*9Be was added through a carrier made at University of Vermont with a concentration of 304 µg mL-1.

**Isotopic analysis was conducted at PRIME Laboratory; ratios were normalized against standard 07KNSTD3110 with an assumed ratio of 2850 x 10-15 (Nishiizumi et al., 2007).

FIGURES
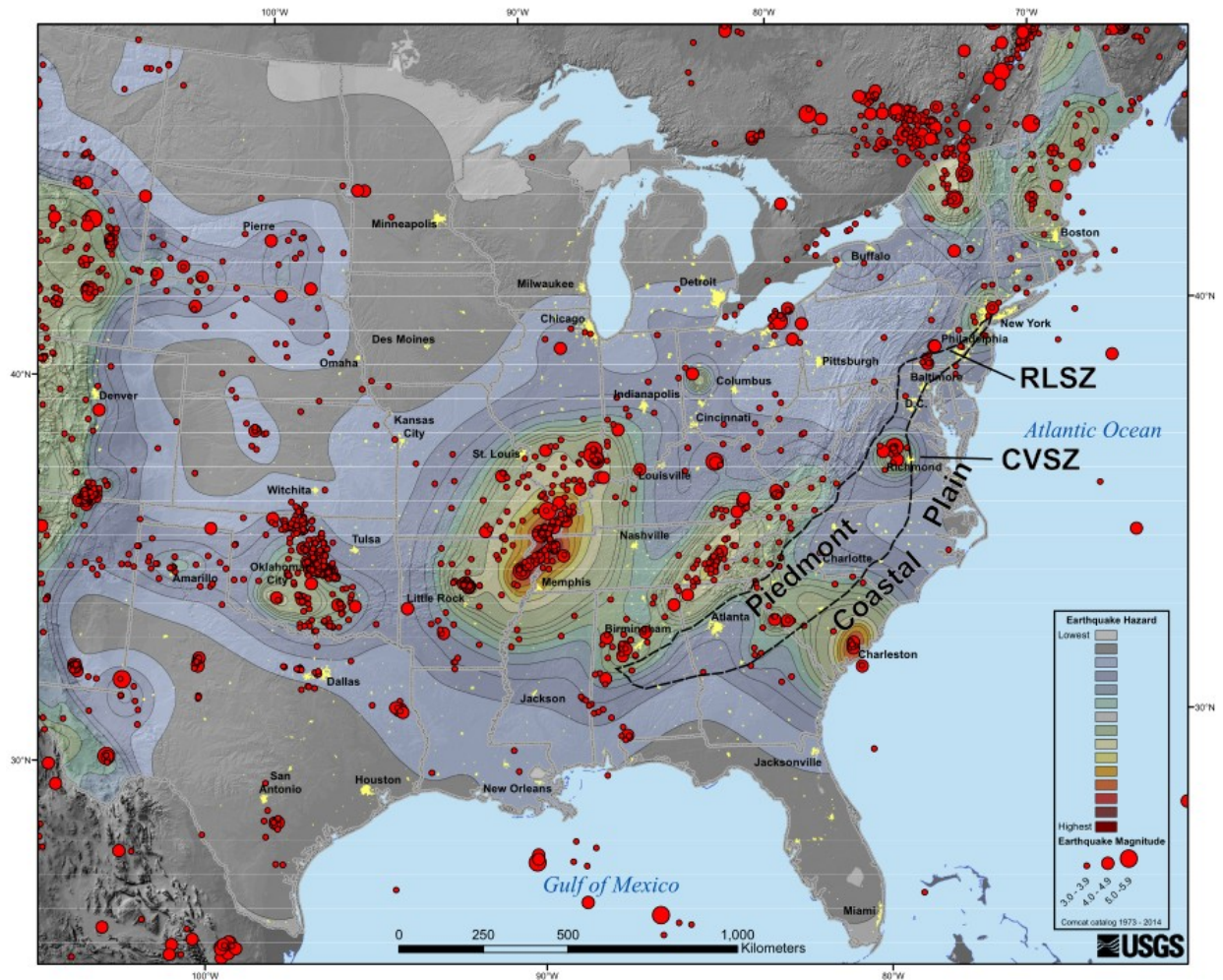
Figure 1. Central and eastern U. S. seismicity and hazard map showing clusters of seismicity interspersed with aseismic regions. Specific to this project, the central Virginia seismic zone (CVSZ) and Reading-Lancaster seismic zone (RLSZ) are labeled. The dashed black outline shows the Piedmont physiographic province, bound on the east by the Coastal Plain, and on the west by the Blue Ridge. (Modified from https://earthquake.usgs.gov/hazards/urban/images/ceus-seis-haz.pdf).
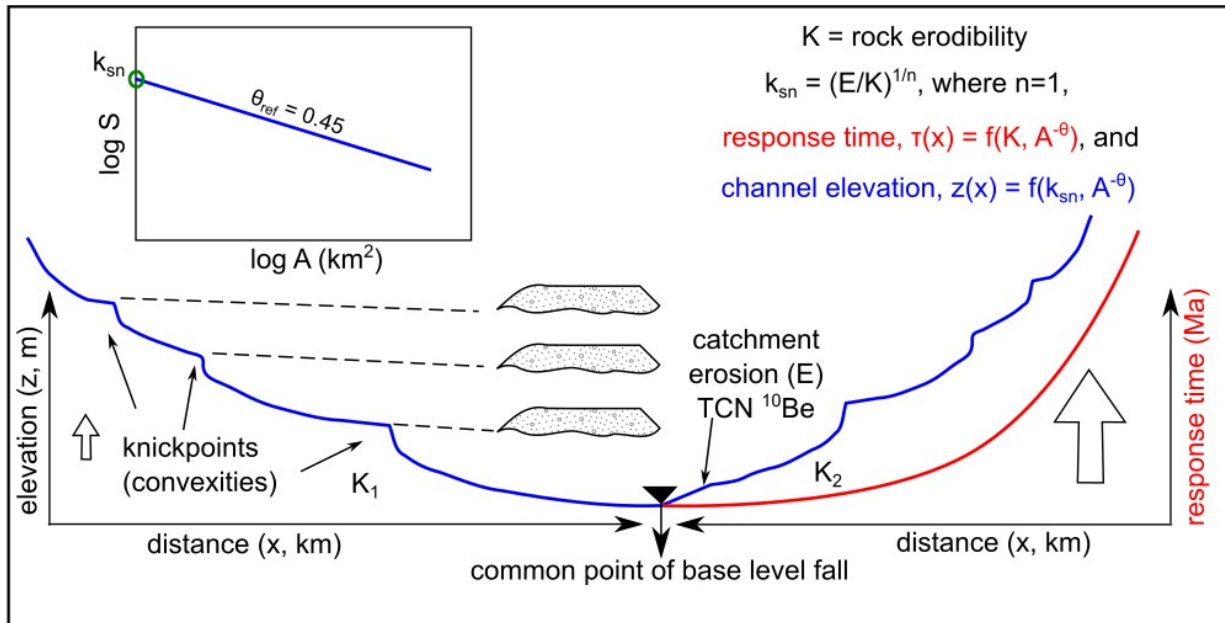
Figure 2. Conceptual strategy in using transient knickpoint geomorphic markers and channel longitudinal profiles as an indicator of crustal strains in the slowly-deforming plate interior. Knickpoints, longitudinal profile steepness (k_{sn}), rock erodibility (K_1, K_2, etc), and basin wide erosion rate (E) are observables that can be modeled using the stream power channel incision to predict the upstream migration of transient knickpoints (response time) and the steady-state channel elevation. A uniform, study-wide stream concavity (θ_{ref}) needs to be adopted to normalize stream steepness. Given that the stream power law predicts that transient knickpoints should rise in elevation at the same rate, given similar rock erodibility, non-uniform knickpoint elevation for catchments that have experienced the same base level fall history indicated by river terraces or related stratigraphic or geomorphic marker, would be an indication of non-uniform rock uplift (small left arrow vs. large right arrow).
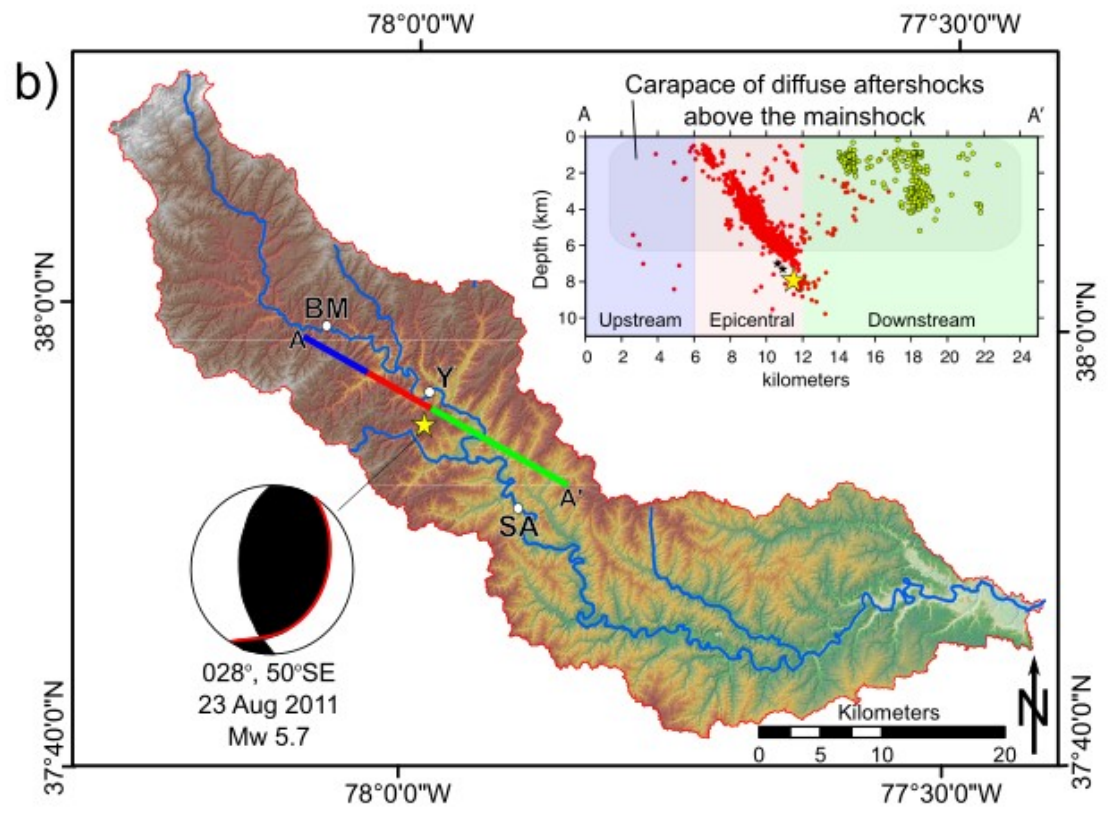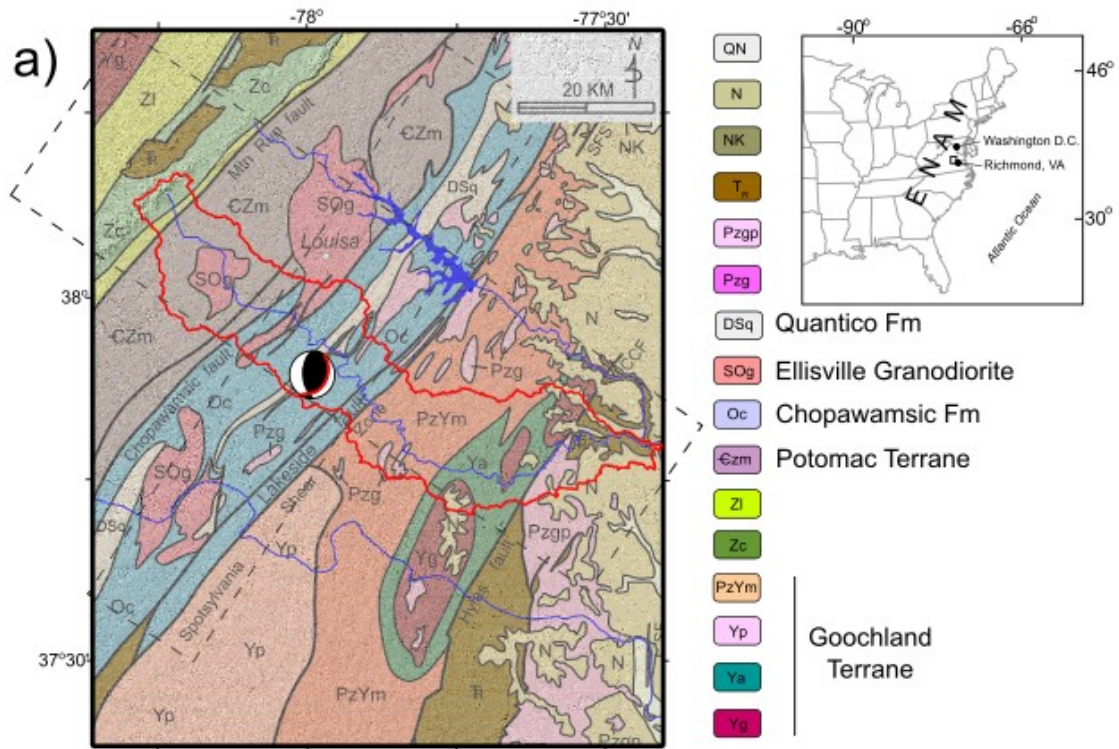
Figure 3. (a) Geologic map of the South Anna and surrounding region showing the location and focal mechanism of the 2011 M_w 5.7 Mineral earthquake. Inset map shows location of the geologic map with respect to Washington D.C. and Richmond, VA in ENAM. Dashed boxes outline locations of the swath profiles in Fig. 4. Yp, Ya, and Yg = Proterozoic granitoids and gneiss; Zl, Zc = Catoctin Formation volcanics; CZm, PzYm = metaclastic passive margin sediments; Oc, Oq, SOg = Taconic metavolcanics and volcaniclastics including the Chopawamsic Formation; Pzg, Pzgp = Paleozoic intrusives; T_R = Mesozoic basin deposits; NK, N, QN = Coastal Plain sediments. (Modified from Pazzaglia et al., 2015). **(b)** Topographic map of the South Anna watershed showing the location and focal mechanism of the Mineral earthquake with the slip plane shown in red. Inset shows the mainshocks (yellow and black stars) and double-difference relocated aftershocks (red and yellow) projected to line A-A' (modified from Wu et al., 2015). The yellow aftershocks are located ~5 km north of the cross section line. Line A-A' is color coded to define the epicentral, upstream, and downstream regions referred to in the text. Locations named in the text and key to maps in Fig. 4 are BM = Byrd Mill, Y = Yancey Mill knickpoint and Yanceyville, SA = South Anna. (Modified from Pazzaglia et al., in press).
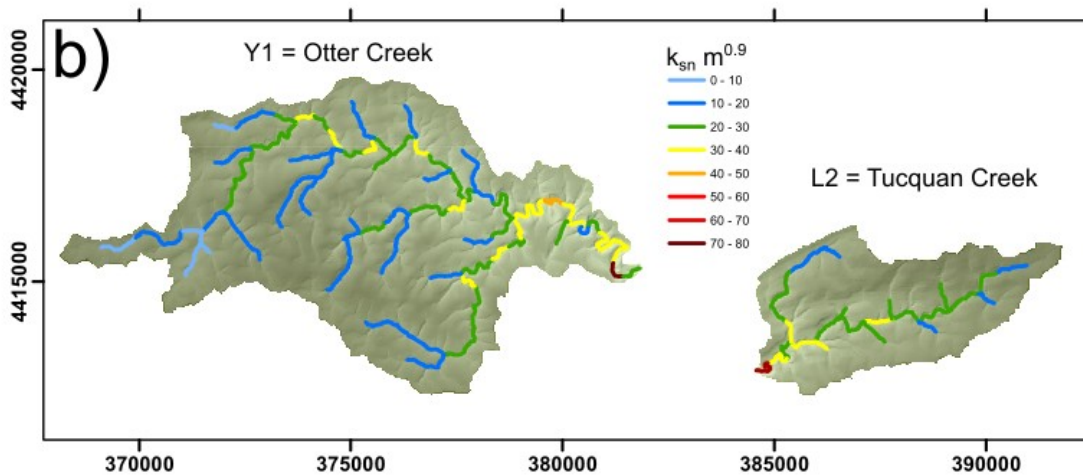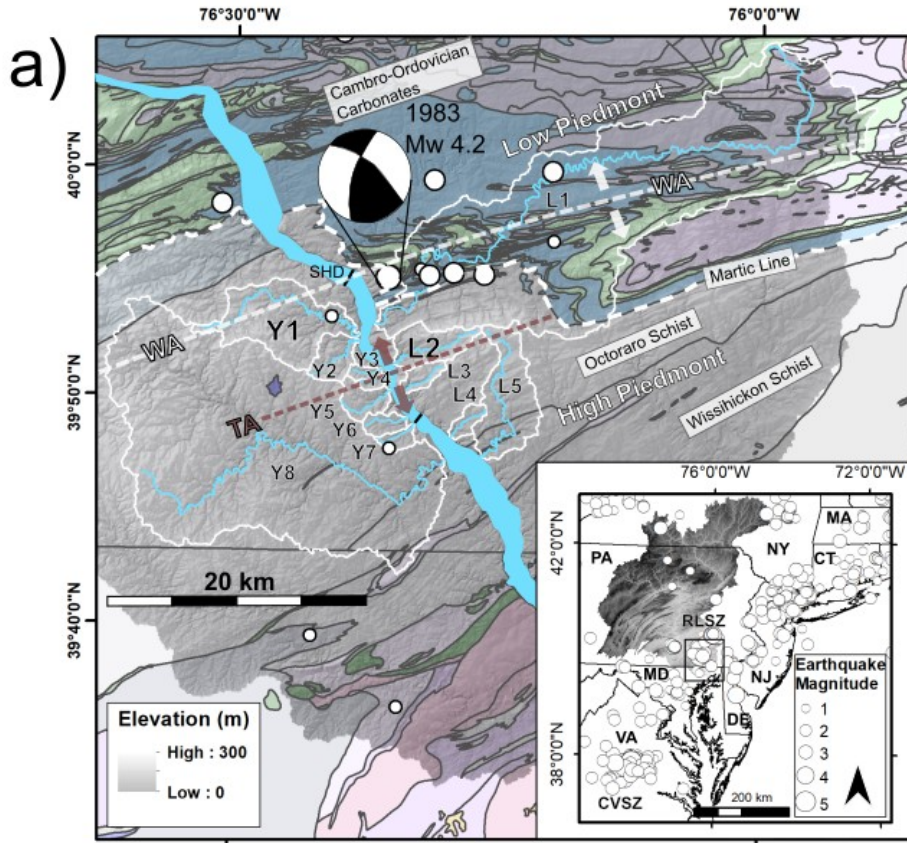
Figure 4. (a) Location map of the Pennsylvania Piedmont study area, underlying geology (USGS) and associated seismicity of the Reading-Lancaster seismic zone (USGS CEUS catalog https://www.sciencebase.gov/catalog/item/5ad7709ce4b0e2c2dd25649c). Watersheds: L1-Pequea Creek, L2- Tucquan Creek, L3- Kelly's Run, L4-Wissler Run, L5- Fishing Creek, Y1-Otter Creek, Y2- Sawmill Run, Y3- Counselman Run, Y4- Duncan Run, Y5- Oakland Run, Y6-Mill Creek, Y7- Anderson Creek, Y8- Muddy Creek. Highlighted is the magnitude 4.3 1984

Lancaster earthquake, which occurred at a depth of 4.5 km on a NNE trending steeply East dipping fault plane (Armbruster and Seeber, 1985; Stockar, 1986). SHD- Safe Harbor Dam, HD-Holtwood Dam. The Tucquan (Freedman et al., 1964) and Westminster (Cambell, 1929) anticlines are Paleozoic structural and Cenozoic topographic features, respectively. Inset: Location of Reading-Lancaster Seismic Zone (RLSZ) and Central Virginia Seismic Zone (CVSZ). (b) Otter Creek and Tucquan Creek catchments are situated on opposing banks of the Susquehanna River and have experienced the same base level fall histories at their mouth. Tucquan Creek drains a portion of Lancaster County proximal to the RLSZ, including the 1983 Lancaster earthquake. Comparable seismicity is lacking beneath otter Creek and in York County PA in general. The steepness (k_{sn}) of the main channels in these watersheds shows that the channels are steepest near their mouths, but that there are several other steep reaches, or knickpoints (see **Fig. 7**).
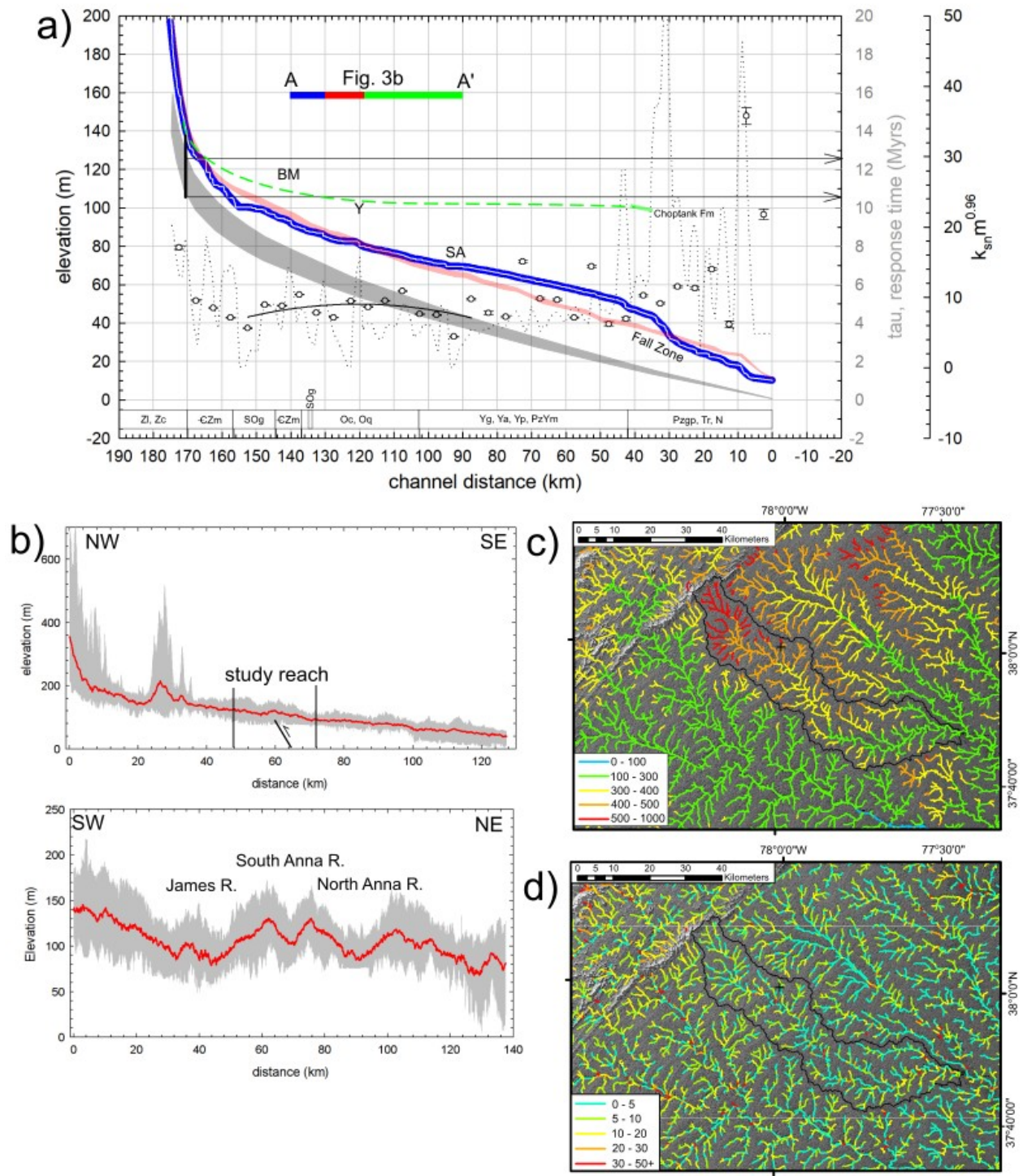
Figure. 5. (a) Long profile of the South Anna River showing the extent of the study area. Actual profile from 10-m DEM in white, smooth profile in dark blue. Dashed green line shows downstream projection of upper profile to Choptank Fm intersection on the inner Coastal Plain.

Black dotted line is channel steepness (k_{sn}) calculated using Eq. 2. Open circles are k_{sn} values calculated over 5 km-long reaches using linear inversion of all South Anna basin channels draining an area > 1 km^2. The short, solid black curve is a polynomial fit to these k_{sn} data through the study reach. Gray shaded curve shows the range of channel response time (Eq. 4) using the minimum and maximum k_{sn} and K values and corresponding arrows indicate the age range for the channel at km 170. Red shaded line is the range of predicted steady-state channel elevations (Eq. 5) using minimum and maximum k_{sn} values. Channel steepness in this plot uses a θ_{ref} = -0.48 Locations keyed to Figures 2 and 4 are same as in Figure 2. Geology traversed by the channel shown in rectangles at the base of the plot with geologic symbols same as in Figure 3a. Location symbols and extent of study reach as in Figure 2b, but the length of the upstream, epicentral, and downstream reaches are longer in this plot because the x-axis is channel distance, not linear distance between A-A'. **(b)** Topographic swath profiles parallel and transverse to the South Anna River. The red line is the mean elevation. **(c)** chi (χ) and **(d)** normalized channel steepness (k_{sn}) of the South Anna and surrounding rivers from a 90-m DEM base and a θ_{ref} = -0.45. (Modified from Pazzaglia et al., in press).
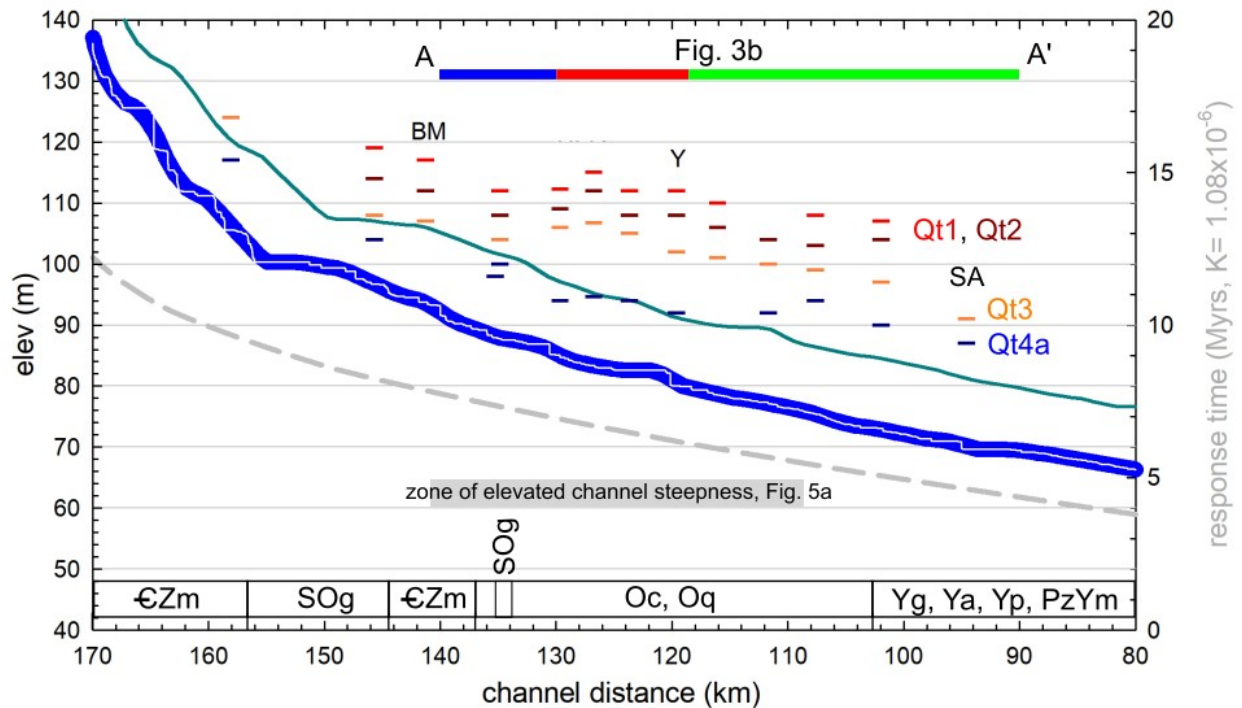
Figure 6. Correlation of mapped and dated terraces, shown as colored dashes, along the South Anna long profile. The raw profile from 10-m DEM data is in white, the smooth profile is the thick blue line. The dashed gray line is the channel response time based on the maximum k_{sn} and K values for the trunk channel keyed into the right vertical axis. The predicted location of the 688 kyr-old Qt3 paleovalley (solid dark cyan line) is keyed into the left vertical axis. Location symbols and extent of study reach as in **Fig.3b**, but the length of the upstream, epicentral, and downstream reaches are longer in this plot because the x-axis is channel distance, not linear distance between A-A'. (Modified from Pazzaglia et al., in press).
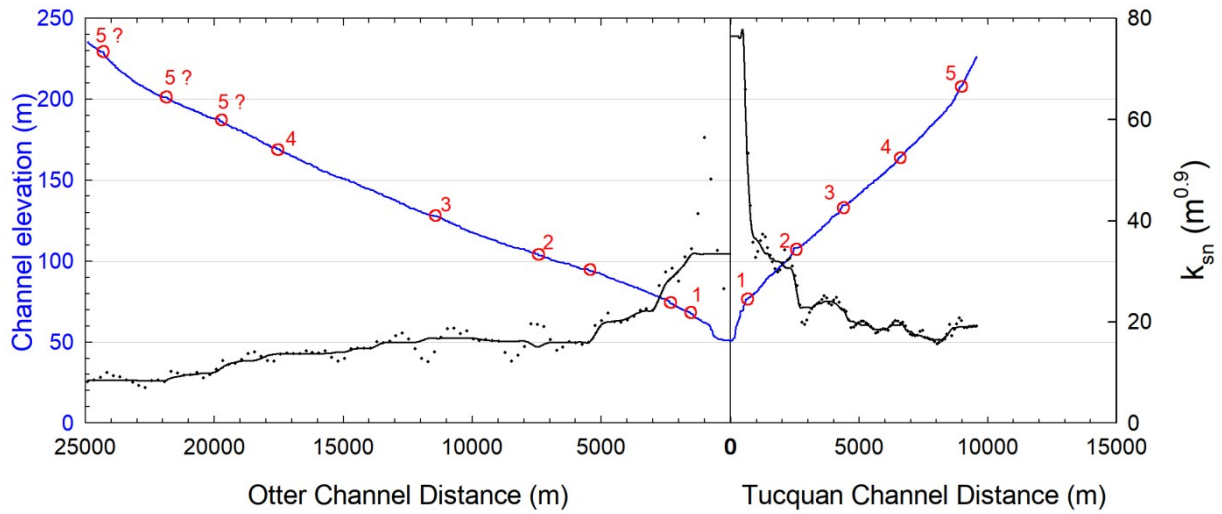
Figure 7. Long profiles (blue) of Otter (left) and Tucquan (right) creeks showing numbered knickpoints (red circles) indicated by peaks in channel steepness (k_{sn}, black dotted line). The solid black line is a smooth interpolation through the k_{sn} data. Channel steepness is calculated with a reference concavity (θ_{ref}) of 0.45. All data derived from a 10-m DEM down-sampled from 1-m resolution LiDAR data.

(a)

(b)
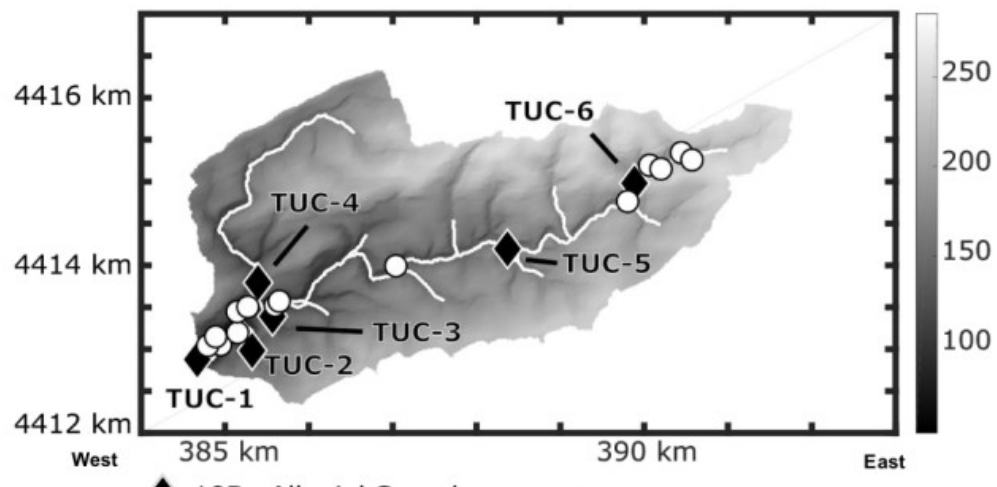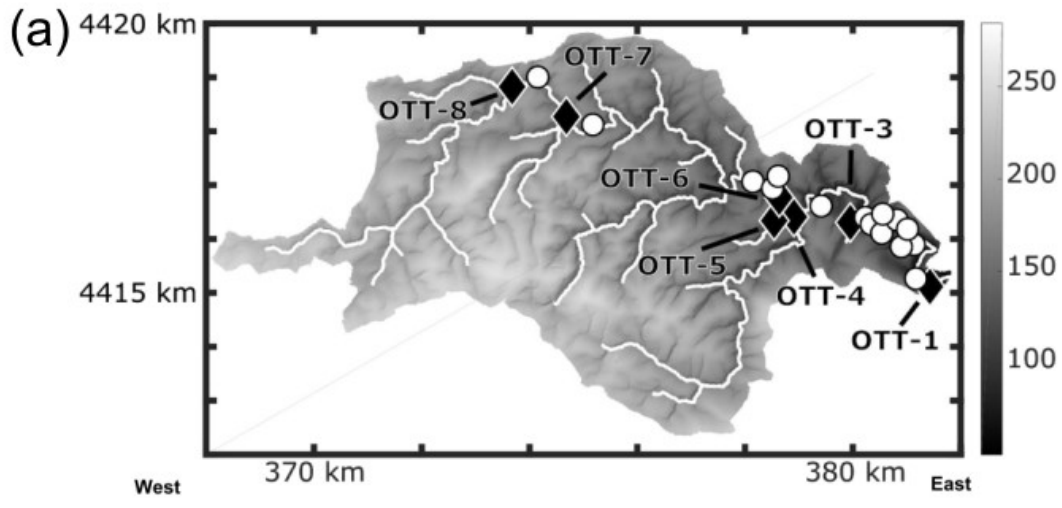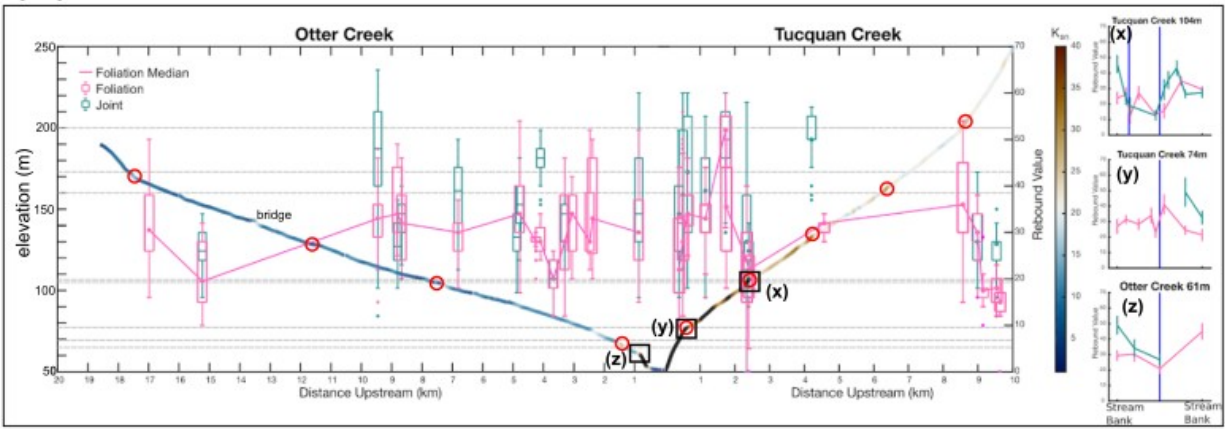
Figure 8. (a) Location of schmidt hammer measurements (white circles) and collection of alluvial material for cosmogenic erosion rates (black diamonds) in the Otter Creek (above) and Tucquan Creek (below) catchments. **(b)** Summary of all rock-hardness and anisotropy field data plotted against the opposing long profiles of Otter and Tucquan creeks. Box and whisker plots show 75% of all data in the box, and 95% in the whisker. Inset plots (x), (y), and (z) are representative channel cross sections showing the distribution of rebound values with respect to the channel middle and channel banks. Channel steepness indicted by color ramp.
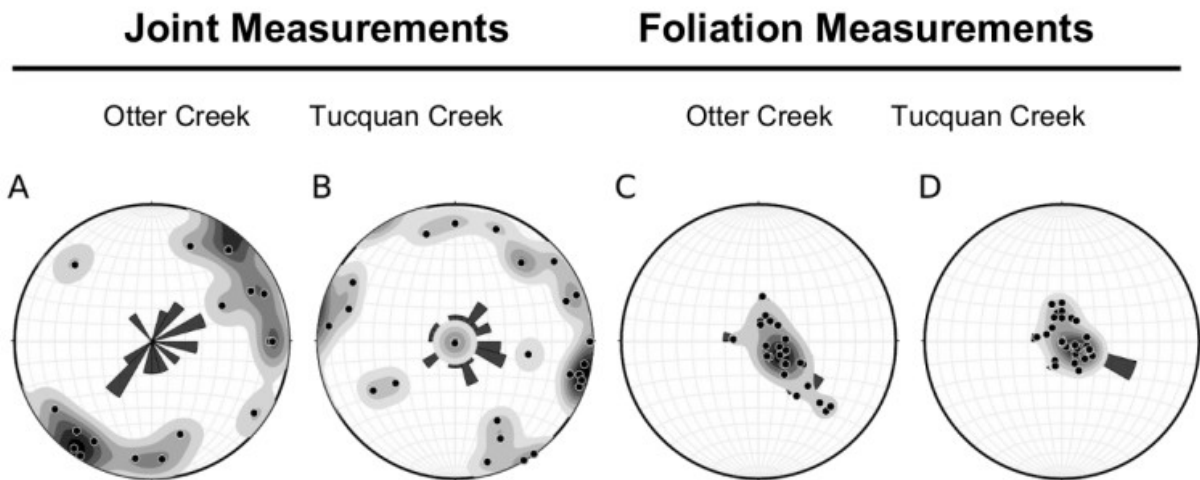
Figure 9. Structural measurements. A, B- Otter Creek (A) joint faces show preferred orientations at 305/85 and 128/85. Tucquan Creek (B) joint faces show a preferred orientation at 195/85. Foliation measurements plotted as the poles to the planes for (C) Otter and (D) Tucquan Creek. F1 foliation surfaces are well-clustered around a mean strike and dip of 202/10.
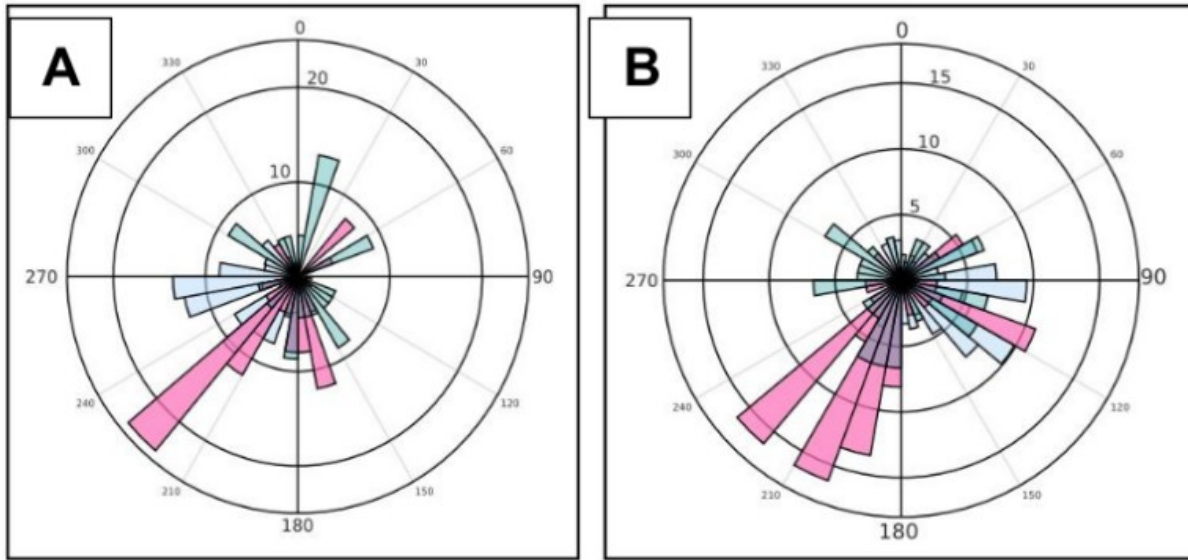
Figure 10. (A) Otter Creek and (B) Tucquan Creek rose diagram plots of foliation strike histogram (red), joint strike histogram (green), and Reach-Length Index (blue). Stream trend is either generally parallel to or orthogonal to foliation.
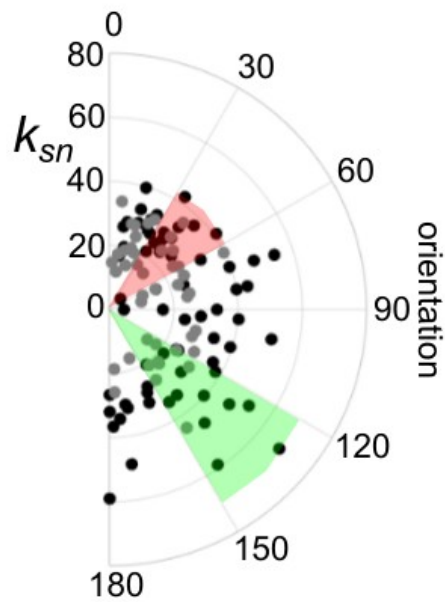
Figure 11. Channel steepness (k_{sn}) in Otter Creek (grey) and Tucquan Creek (Black) against stream orientation. The lowest channel steepness values are generally subparallel to the dominate foliation (in red shading) whereas the highest steepness values are orthogonal to the channel steepness, and subparallel to the dominant joint orientations (green shading).
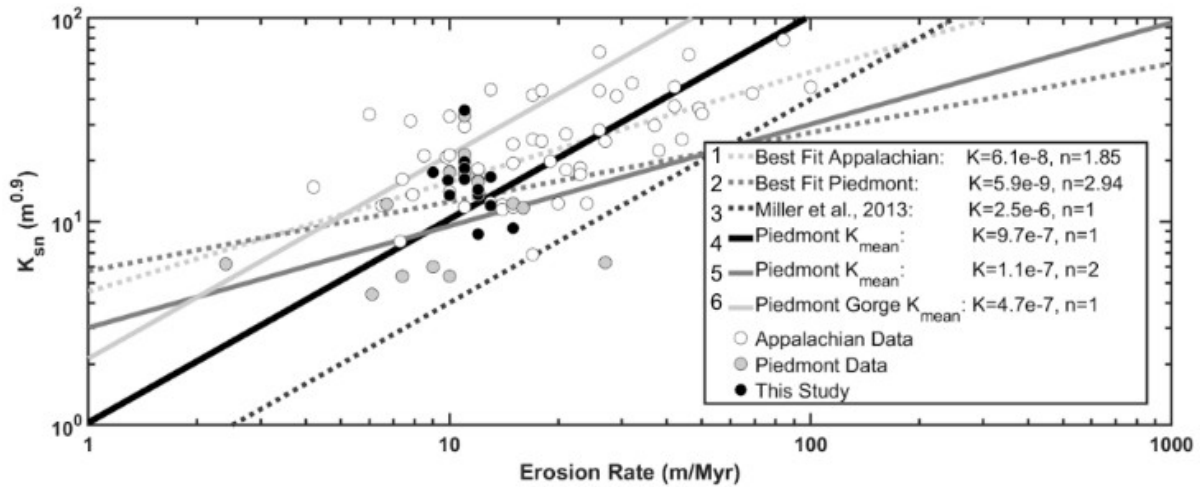
Figure 12. Stream steepness – erosion rate plot with regressions derived from (1) the full Appalachian global erosion rate dataset (Kirby and Whipple, 2012; Miller 2013), (2) only the data taken from the Appalachian Piedmont, (3) the Miller et al. (2013) modeled best fit representing the Susquehanna River basin, (4) direct application of eq. (3) on Piedmont data forcing n=1, (5) direct application of eq. 13 on Piedmont data forcing n=2, (6) direct application of eq. (3) on data from the steeply incised valleys of the Susquehanna Piedmont. K and n from (4) is used for further modeling in this study.
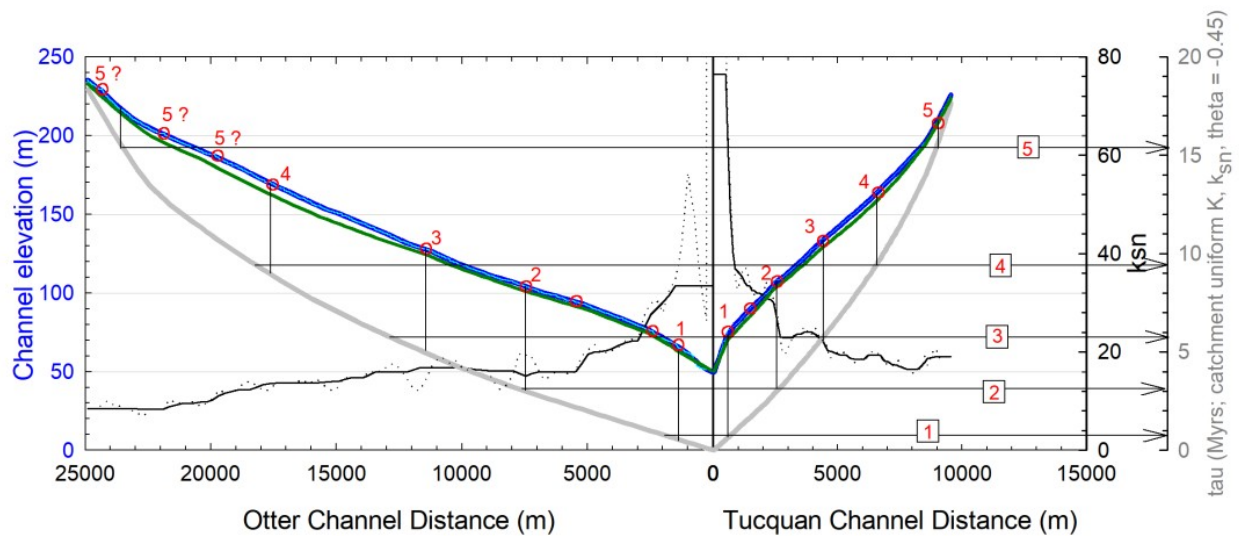
Figure 13. Response times (gray lines) and model predicted channel elevation (green lines) based on the longitudinal profiles of Fig. 7 and a catchment uniform k_{sn} and K. The elevation of several knickpoints in the Tucquan Creek channel do not have a corresponding-elevation knickpoint in the Otter Creek drainage, consistent with more rock uplift beneath Tucquan Creek, as envisioned in **Fig. 2**. Modeled knickpoint response times are consistent with the history of base level fall and stratigraphic markers preserved in the Lower Susquehanna River basin (Pazzaglia, 1993; Pazzaglia and Gardner, 1993).
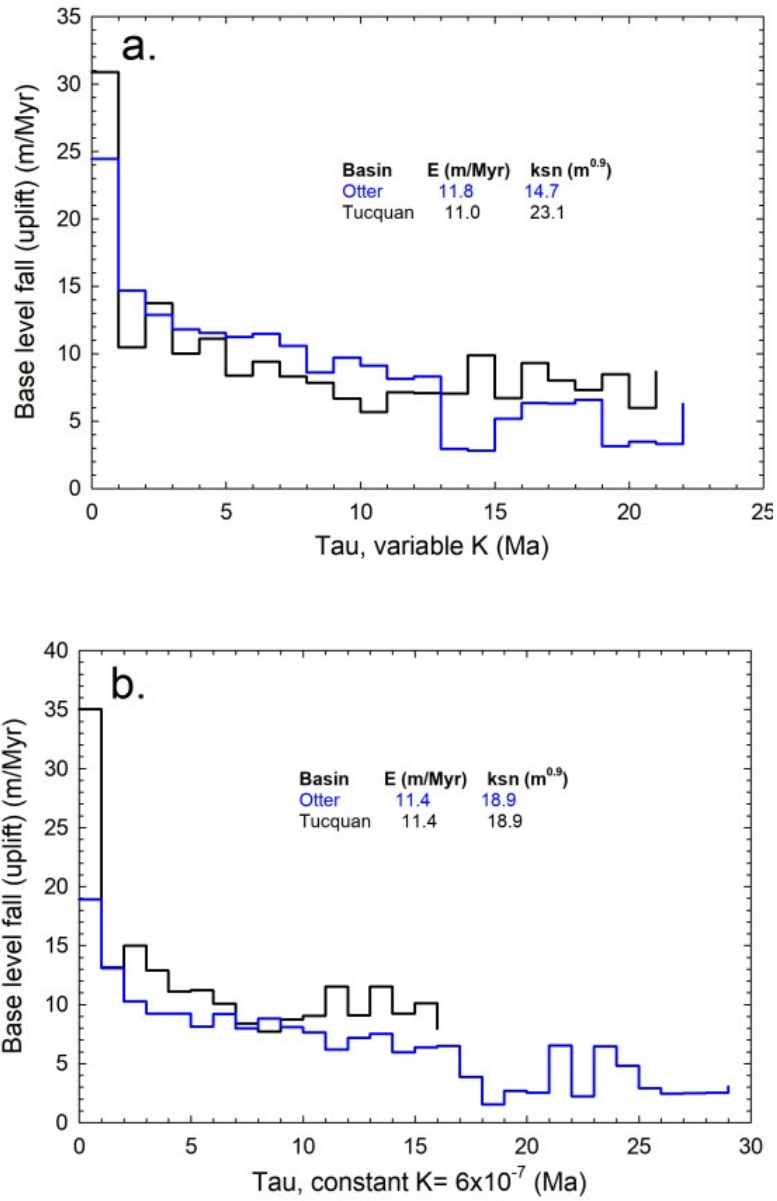
Figure 14. Modeled base level fall histories for Otter (blue) and Tucquan (black) creeks assuming **(a)** catchment uniform k_{sn} and erosion rate, and **(b)** Piedmont uniform k_{sn} and erosion rate. Note how Tucquan Creek has systematically experienced greater base level fall in the **(b)** simulation.
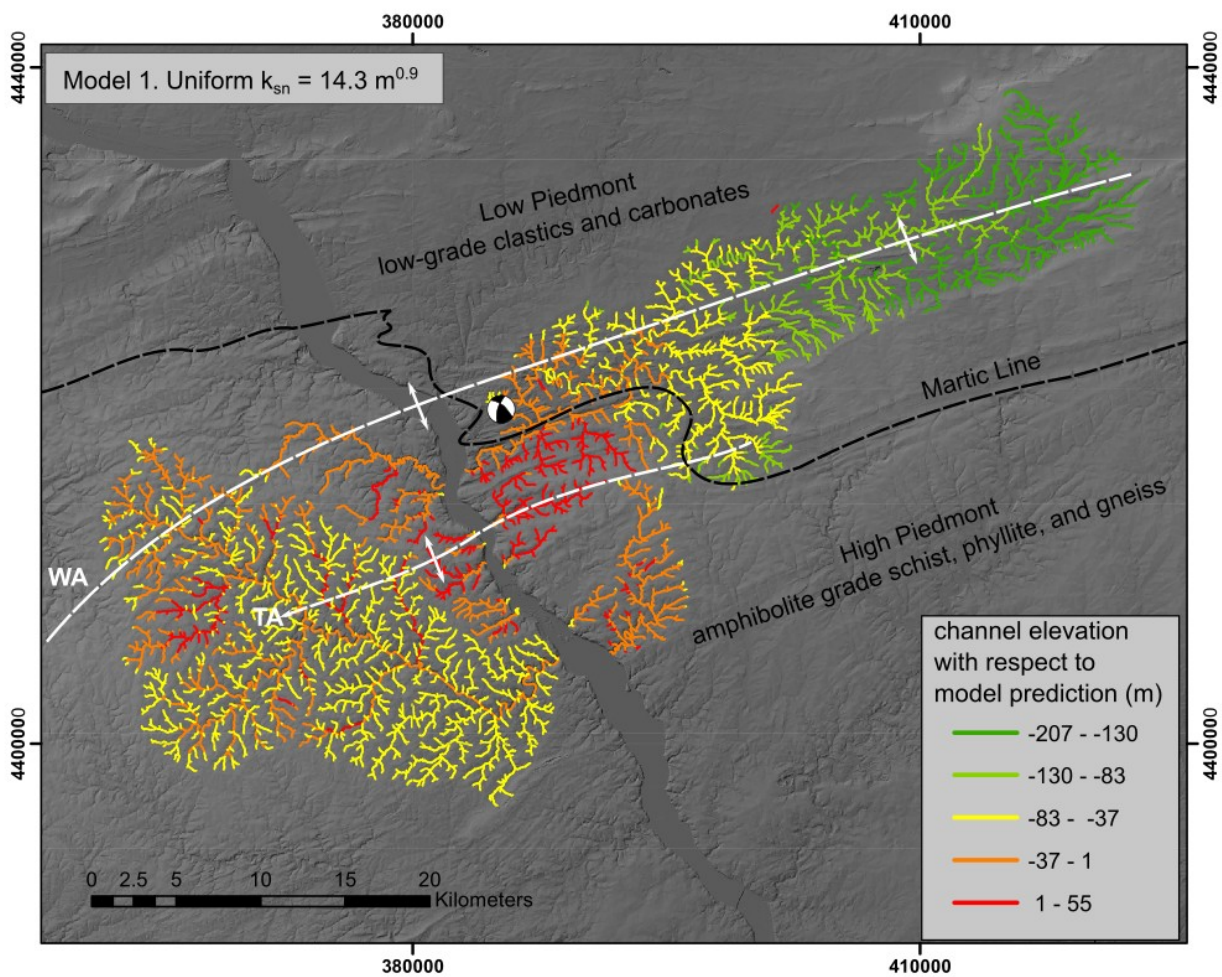
Figure 15. Piedmont-wide model results of predicted channel elevation using a single, uniform steepness value for all channels. WA = Westminster Anticline (Campbell, 1929). TA = Tucquan Anticline (Freedman et al., 1994). Focal mechanism is location of 1983 Lancaster earthquake.
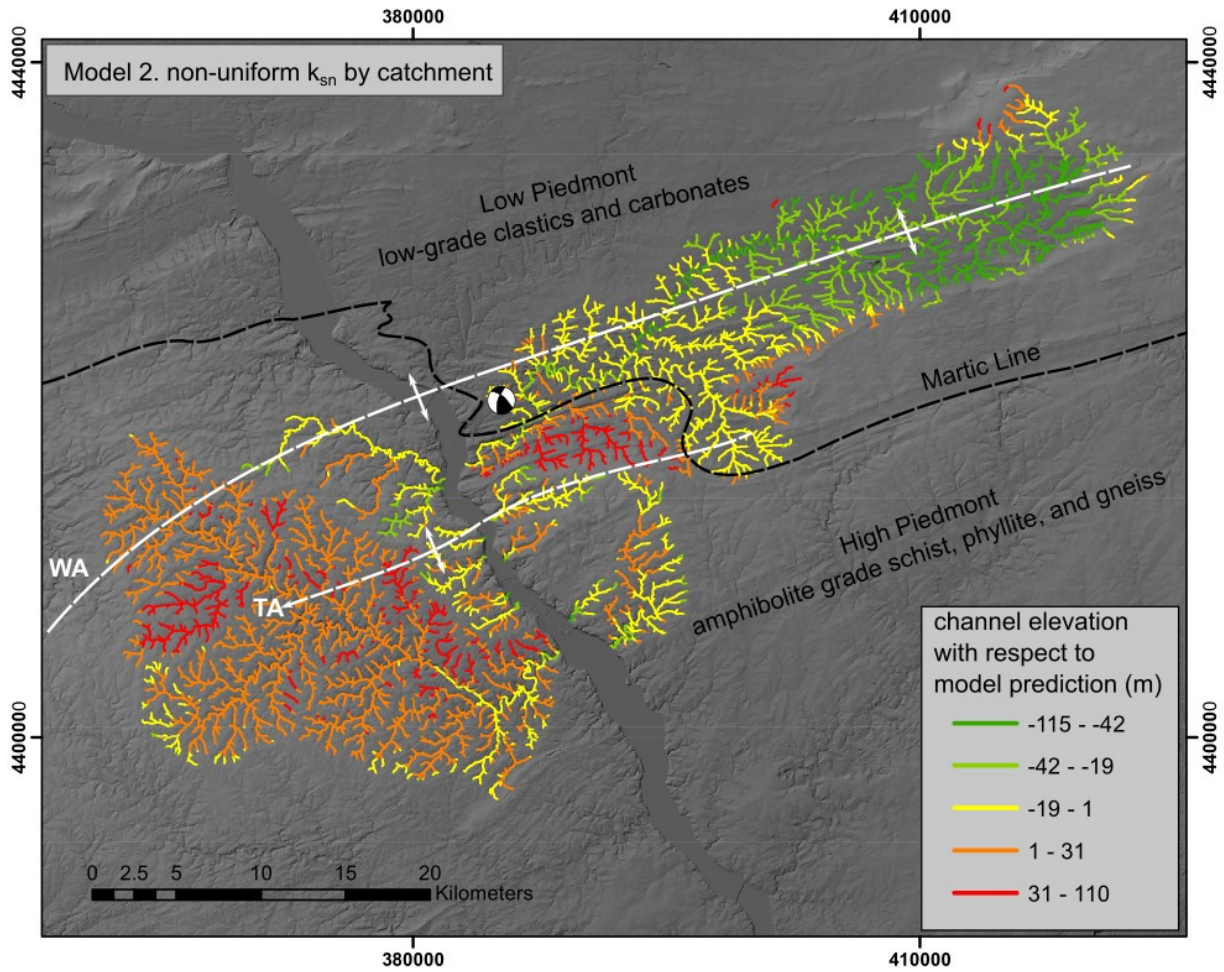
Figure 16. Piedmont-wide model results of predicted channel elevation using a non-uniform channel steepness calculated as the median for each catchment. WA = Westminster Anticline (Campbell, 1929). TA = Tucquan Anticline (Freedman et al., 1994). Focal mechanism is location of 1983 Lancaster earthquake.
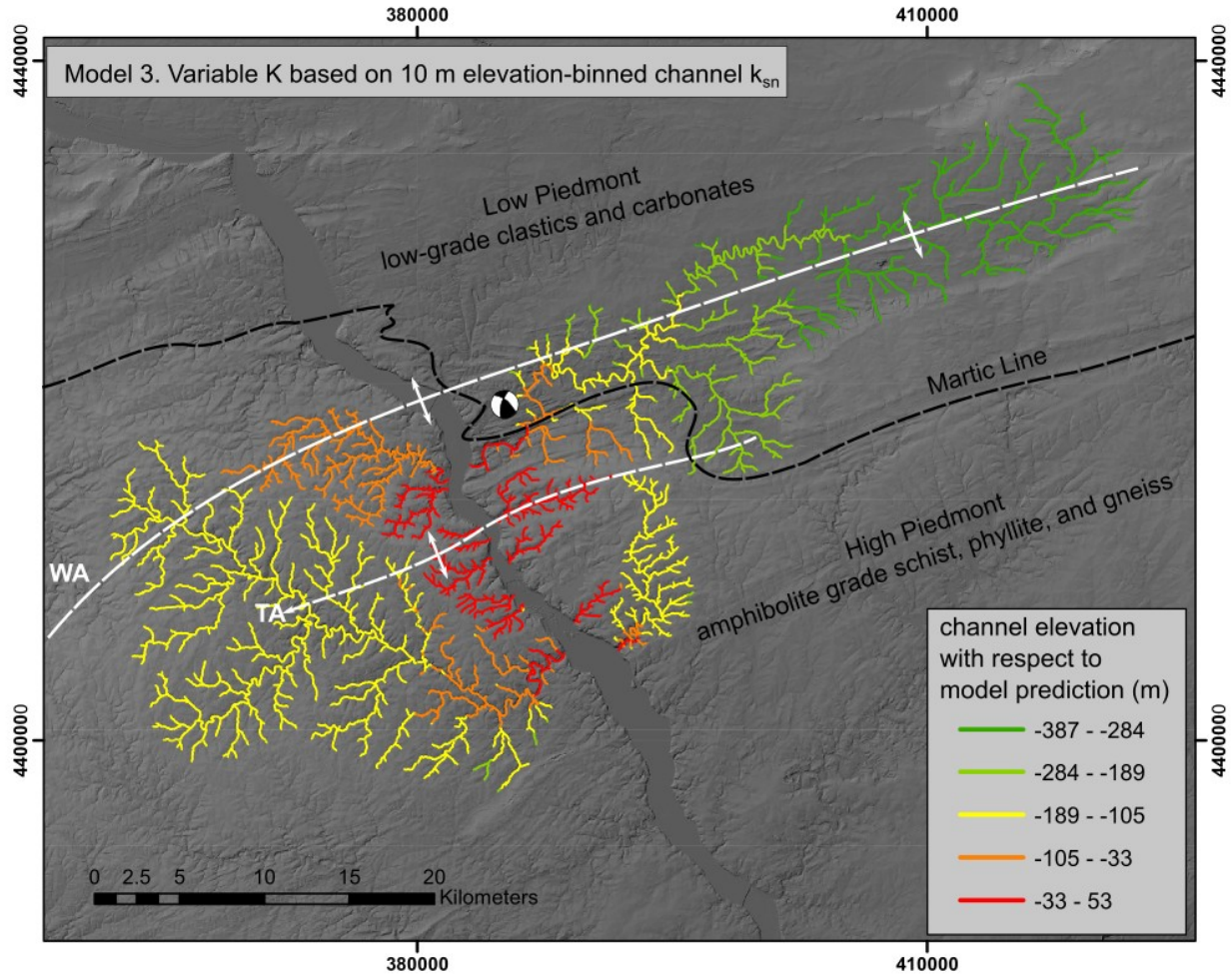
Figure 17. Piedmont-wide model results of predicted channel elevation using a non-uniform channel steepness calculated for 10-m bin elevations of all channels. WA = Westminster Anticline (Campbell, 1929). TA = Tucquan Anticline (Freedman et al., 1994). Focal mechanism is location of 1983 Lancaster earthquake.

Appendix A. Schmidt Hammer and Structural Measurements

Schmidt Hammer Joint Measurements

Otter Creek

Mean RV: 35
St. Devation 10

Sample	Mean RV	St. Deviation	St. Error	Latitude	Longitude	Elevation	Strike	Dip	Downstream Trend	N
OC-01-J1	49	6	1	39.8786585	- 76.389537	62	302	88	155	30
OC-01-J2	34	5	1	39.8786585	- 76.389537	62	306	86	155	30
OC-01-J3	27	3	1	39.8786585	- 76.389537	62	45	68	155	30
OC-02-J1	32	5	1	39.8891919	- 76.402019	95	253	60	75	30
OC-02-J2	20	4	1	39.8891919	- 76.402019	95	180	75	75	30
OC-03-J1	46	4	1	39.8887403	- 76.401067	95	112	64	80	30
OC-05-J1	36	6	1	39.8868718	- 76.39738	90	310	74	75	30
OC-06-J1	26	4	1	39.8886909	- 76.394106	90	180	77	135	30
OC-10-F1	32	6	1	39.8893028	- 76.395881	85	215	80	50	30
OC-11-J1	38	7	1	39.8908124	- 76.411389	102	325	75	130	30
OC-22-J1	33	5	1	39.8944945	- 76.425117	115	130	76	90	30
OC-12-J2	32	5	1	39.8944945	- 76.425117	115	130	76	90	30
OC-13-J1	28	6	1	39.8936976	- 76.420649	113	153	48	360	30
OC-14-J1	54	10	2	39.8949228	- 76.420085	110	278	75	128	30
OC-14-J2	41	9	2	39.8949228	- 76.420085	110	300	73	128	30
OC-15-J1	26	4	1	39.9033755	- 76.461384	140	153	70	55	30

Tucquan Creek

Mean RV: 34
St. Devation: 12

Sample	Mean RV	St. Deviation	St. Error	Latitude	Longitude	Elevation	Strike	Dip	Downstream Trend	N
TC-01-J2	34	3	1	39.8590233	- 76.345935	70	110	76	125	30
TC-01-J3	23	4	1	39.8590233	- 76.345935	70	30	75	125	30
TC-01-J4	42	6	1	39.8590233	- 76.345935	70	160	75	125	30
TC-02-J1	49	9	2	39.8590806	- 76.346769	75	7	82	105	30
TC-02-J2	33	4	1	39.8590806	- 76.346769	75	90	75	105	30
TC-03-J1	29	6	1	39.8598907	- 76.346638	77	242	55	240	30
TC-03-J2	55	4	1	39.8598907	- 76.346638	77	17	70	240	30
TC-05-J1	30	3	1	39.8611568	- 76.342524	85	240	90	340	30
TC-05-J2	43	7	1	39.8611568	- 76.342524	85	190	85	340	30
TC-05-J3	43	9	2	39.8611568	- 76.342524	85	329	59	340	30
TC-06-J1	52	5	1	39.8633123	- 76.342605	94	195	83	176	30
TC-06-J2	49	9	2	39.8633123	- 76.342605	94	75	70	176	30
TC-08-J1	46	5	1	39.8637008	- 76.33796	104	122	0	235	30
TC-08-J2	24	4	1	39.8637008	- 76.33796	104	200	86	235	30
TC-08-J3	19	5	1	39.8637008	- 76.33796	104	197	86	235	30
TC-08-J4	13	3	1	39.8637008	- 76.33796	104	130	64	235	30
TC-08-J5	29	6	1	39.8637008	- 76.33796	104	141	82	235	30
TC-08-J6	36	5	1	39.8637008	- 76.33796	104	255	80	235	30
TC-08-J7	43	5	1	39.8637008	- 76.33796	104	180	88	235	30
TC-08-J8	27	2	0	39.8637008	- 76.33796	104	325	44	235	30
TC-08-J9	27	3	1	39.8637008	- 76.33796	104	130	64	235	30
TC-09-J1	26	6	1	39.8638051	- 76.337858	107	196	76	280	30
TC-09-J2	27	2	0	39.8638051	- 76.337858	107	245	67	280	30
TC-09-J3	22	3	1	39.8638051	- 76.337858	107	235	90	280	30
TC-10-J2	51	5	1	39.8671392	- 76.32396	140	159	84	320	30
TC-12-J1	29	7	1	39.8792954	- 76.286221	215	190	45	292	30
TC-13-J1	26	5	1	39.8804989	- 76.280678	232	280	1	280	30

Schmidt Hammer Foliation Measurements

Otter Creek

Mean RV: 31
St. Deviation: 9

Sample	Mean RV	St. Deviation	St. Error	Latitude	Longitude	Elevation	Strike	Dip	Downstream Trend	N
OC-01-F1	37	8	1	39.8786585	- 76.389537	62	95	12	155	30
OC-01-F2	27	4	1	39.8786585	- 76.389537	62	97	10	155	30
OC-01-F3	15	3	1	39.8786585	- 76.389537	62	105	16	155	30
OC-01-F4	26	4	1	39.8786585	- 76.389537	62	95	27	155	30
OC-03-F1	33	5	1	39.8887403	- 76.401067	95	175	16	80	30
OC-04-F1	34	6	1	39.8874044	- 76.398731	92	210	5	155	30
OC-05-F1	32	6	1	39.8868718	- 76.39738	90	195	13	75	30
OC-06-F1	37	5	1	39.8886909	- 76.394106	90	5	15	135	30
OC-06-F2	36	7	1	39.8886909	- 76.394106	90	5	15	135	30
OC-07-F1	23	2	0	39.8842742	- 76.391357	75	235	11	60	30
OC-07-F2	31	3	1	39.8842742	- 76.391357	75	235	11	60	30
OC-08-F1	43	5	1	39.8836432	- 76.39233	80	120	14	50	30
OC-08-F2	27	4	1	39.8836432	- 76.39233	80	140	15	50	30
OC-09-F1	32	3	1	39.8859612	- 76.391491	80	240	10	170	30
OC-10-F1	36	8	2	39.8893028	- 76.395881	85	200	17	50	30
OC-11-F1	28	2	0	39.8908124	- 76.411389	102	210	15	130	30
OC-11-F2	29	3	1	39.8908124	- 76.411389	102	210	15	130	30
OC-12-F1	20	4	1	39.8944945	- 76.425117	115	232	25	90	30
OC-12-F2	21	5	1	39.8944945	- 76.425117	115	212	15	90	30
OC-12-F3	38	6	1	39.8944945	- 76.425117	115	222	20	90	30
OC-13-F1	33	7	1	39.8936976	- 76.420649	113	207	30	358	30
OC-13-F2	38	7	1	39.8936976	- 76.420649	113	207	28	359	30
OC-14-F1	26	2	0	39.8949228	- 76.420085	110	220	21	128	30
OC-14-F2	43	8	1	39.8949228	- 76.420085	110	220	21	128	30
OC-14-F3	27	5	1	39.8949228	- 76.420085	110	198	17	128	30
OC-15-F1	29	3	1	39.9033755	- 76.461384	140	225	53	55	30
OC-15-F2	30	5	1	39.9033755	- 76.461384	140	222	40	55	30
OC-16-F1	21	3	1	39.9059165	- 76.456127	140	235	40	5	30
OC-17-F1	45	5	1	39.9111463	- 76.472959	160	226	60	95	30
OC-17-F2	31	9	0	39.9111463	- 76.472959	160	222	60	95	30

Tucquan Creek

Mean RV: 30
St. Devation: 12

Sample	Mean RV	St. Deviation	St. Error	Latitude	Longitude	Elevation	Strike	Dip	Downstream Trend	N
TC-01-F1	18	21	3	39.8590233	- 76.345935	70	86	18	125	30
TC-01-F2	43	36	5	39.8590233	- 76.345935	70	112	15	125	30
TC-01-F3	21	16	2	39.8590233	- 76.345935	70	125	15	125	30
TC-02-F1	36	21	4	39.8590806	- 76.346769	75	170	15	105	30
TC-02-F2	16	25	3	39.8590806	- 76.346769	75	80	17	105	30
TC-02-F3	21	41	6	39.8590806	- 76.346769	75	90	23	105	30
TC-02-F4	25	23	3	39.8590806	- 76.346769	75	72	15	105	30
TC-02-F5	41	34	5	39.8590806	- 76.346769	75	90	0	105	30
TC-02-F6	23	28	3	39.8590806	- 76.346769	75	90	18	105	30
TC-02-F7	34	31	3	39.8590806	- 76.346769	75	90	14	105	30
TC-02-F8	28	27	4	39.8590806	- 76.346769	75	75	23	105	30
TC-03-F1	31	31	3	39.8598907	- 76.346638	77	10	15	240	30
TC-03-F2	27	39	5	39.8598907	- 76.346638	77	205	20	240	30
TC-05-F1	39	34	5	39.8611568	- 76.342524	85	226	12	340	30
TC-05-F2	21	30	4	39.8611568	- 76.342524	85	240	20	340	30
TC-05-F3	34	35	6	39.8611568	- 76.342524	85	55	10	340	30
TC-06-F1	35	41	4	39.8633123	- 76.342605	94	206	12	176	30
TC-06-F2	29	54	4	39.8633123	- 76.342605	94	217	17	176	30
TC-06-F3	41	53	5	39.8633123	- 76.342605	94	230	4	176	30
TC-07-F1	54	35	10	39.8634579	- 76.342554	95	210	8	176	30
TC-08-F1	15	24	4	39.8637008	- 76.33796	104	75	1	235	30
TC-08-F2	32	26	4	39.8637008	- 76.33796	104	203	10	235	30
TC-08-F3	24	12	5	39.8637008	- 76.33796	104	190	15	235	30
TC-08-F4	26	27	4	39.8637008	- 76.33796	104	205	20	235	30
TC-08-F5	12	13	2	39.8637008	- 76.33796	104	200	16	235	30
TC-08-F6	27	16	5	39.8637008	- 76.33796	104	198	17	235	30
TC-08-F7	13	35	3	39.8637008	- 76.33796	104	200	11	235	30
TC-08-F8	16	30	2	39.8637008	- 76.33796	104	198	17	235	30
TC-09-F1	35	8	5	39.8638051	- 76.337858	107	200	8	280	30
TC-09-F2	30	22	5	39.8638051	- 76.337858	107	200	8	280	30
TC-09-F3	8	21	3	39.8638051	- 76.337858	107	222	11	280	30
TC-09-F4	22	22	4	39.8638051	- 76.337858	107	205	10	280	30
TC-09-F5	21	25	2	39.8638051	- 76.337858	107	196	17	280	30
TC-11-F1	39	30	4	39.8685517	- 76.320705	137	250	1	210	30
TC-12-F5	25	20	3	39.8792954	- 76.286221	215	195	8	292	30
TC-12-F6	29	28	3	39.8792954	- 76.286221	215	240	15	292	30
TC-12-F7	20	29	5	39.8792954	- 76.286221	215	290	12	292	30
TC-13-F1	28	18	3	39.8804989	- 76.280678	232	25	10	280	30
TC-14-F1	29	15	3	39.8805098	- 76.279931	235	210	0	225	30
TC-15-F1	18	17	3	39.8794125	- 76.284492	218	0	0	255	30
TC-16-F1	37	9	3	39.8766292	- 76.287984	200	285	15	165	30

Appendix B. TCN 10 Be results.

Blank Name	UVM Batch Number	Cathode Number	Be Analysis Date	From AMS: $^{10}Be/^{9}Be$ Ratio	From AMS: $^{10}Be/^{9}Be$ Ratio Uncertainty
BLKXX	642	151637	12/6/2018	5.036E-15	7.696E-16
BLK	644	151642	12/6/2018	4.035E-15	1.264E-15
			AVERAGE	**4.536E-15**	
			STDEV	**7.081E-16**	

We had two batches of samples (yours and another visitor's) that were prepared at about the same time, in the same hood, on the same 9Be carrier, and run on the AMS at the same time. So my suggestion would be to use the average of those two blanks in order to get better statistical control on the blank uncertainty. We can certainly discuss other options, although it honestly won't matter much since the blank is two orders of magnitude lower than your samples and the correction will be trivial.

CONSTANTS

Density of ^{9}Be Carrier (g/mL):	1.012
Atomic Mass of Be (g/mol):	9.012182
Avogadro's Number (atoms/mol):	6.022E+23

SAMPLE PREPARATION DATA

Sample Name	UVM Batch Number	Be Analysis Date	Quartz Mass (g)	Mass of ^{9}Be Carrier Added (g)	Concentration of ^{9}Be Carrier Added (µg/mL)	Calculate: ^{9}Be Atoms Added
OTT-1	644	12/6/2018	21.9185	0.8333	304	1.673E+19
OTT-3	644	12/6/2018	23.0931	0.8325	304	1.671E+19
OTT-4	644	12/6/2018	21.9522	0.8303	304	1.667E+19
OTT-6	644	12/6/2018	21.8800	0.8310	304	1.668E+19
OTT-7	644	12/6/2018	21.8210	0.8310	304	1.668E+19
TUC-1	644	12/6/2018	21.9741	0.8280	304	1.662E+19
TUC-2	644	12/6/2018	21.9804	0.8306	304	1.667E+19
TUC-3	644	12/6/2018	17.2038	0.8313	304	1.669E+19
TUC-4	644	12/6/2018	21.9737	0.8283	304	1.663E+19
TUC-5	644	12/6/2018	22.0228	0.8252	304	1.656E+19

CALCULATIONS TO DETERMINE CONCENTRATION

Sample Name	From AMS: Uncorrected ^{10}Be/^{9}Be Ratio	From "Blanks" Sheet: Background ^{10}Be/^{9}Be Ratio	Calculate: Background-Corrected ^{10}Be/^{9}Be Ratio	Calculate: ^{10}Be Atoms	Calculate: ^{10}Be Atoms/g
OTT-1	4.513E-13	4.536E-15	4.468E-13	7.473E+06	3.409E+05
OTT-3	6.192E-13	4.536E-15	6.147E-13	1.027E+07	4.448E+05
OTT-4	5.281E-13	4.536E-15	5.236E-13	8.726E+06	3.975E+05
OTT-6	4.496E-13	4.536E-15	4.450E-13	7.423E+06	3.393E+05
OTT-7	3.879E-13	4.536E-15	3.834E-13	6.395E+06	2.931E+05
TUC-1	4.686E-13	4.536E-15	4.641E-13	7.713E+06	3.510E+05
TUC-2	4.655E-13	4.536E-15	4.609E-13	7.685E+06	3.496E+05
TUC-3	3.980E-13	4.536E-15	3.935E-13	6.566E+06	3.817E+05
TUC-4	4.414E-13	4.536E-15	4.368E-13	7.263E+06	3.305E+05
TUC-5	5.457E-13	4.536E-15	5.411E-13	8.963E+06	4.070E+05

CALCULATIONS TO DETERMINE UNCERTAINTY

Sample Name	From AMS: Uncorrected ^{10}Be/^{9}Be Ratio Uncertainty	From "Blanks" Sheet: Background ^{10}Be/^{9}Be Ratio Uncertainty	Calculate: Background-Corrected ^{10}Be/^{9}Be Ratio Uncertainty	Calculate: Uncertainty ^{10}Be Atoms	Calculate: Uncertainty ^{10}Be Atoms/g
OTT-1	1.043E-14	7.081E-16	1.045E-14	1.749E+05	7.978E+03
OTT-3	1.505E-14	7.081E-16	1.507E-14	2.518E+05	1.090E+04
OTT-4	1.136E-14	7.081E-16	1.139E-14	1.898E+05	8.644E+03
OTT-6	1.071E-14	7.081E-16	1.073E-14	1.790E+05	8.180E+03
OTT-7	8.755E-15	7.081E-16	8.783E-15	1.465E+05	6.714E+03
TUC-1	1.036E-14	7.081E-16	1.039E-14	1.726E+05	7.855E+03
TUC-2	1.237E-14	7.081E-16	1.239E-14	2.066E+05	9.398E+03
TUC-3	1.083E-14	7.081E-16	1.085E-14	1.811E+05	1.053E+04
TUC-4	1.185E-14	7.081E-16	1.187E-14	1.974E+05	8.982E+03
TUC-5	1.283E-14	7.081E-16	1.285E-14	2.128E+05	9.662E+03

Sample Name	Quartz Mass (g)	Mass of ^{9}Be Added (μg)*	AMS Cathode Number	Uncorrected ^{10}Be/^{9}Be Ratio**	Uncorrected ^{10}Be/^{9}Be Ratio Uncertainty**	Background-Corrected ^{10}Be/^{9}Be Ratio	Background-Corrected ^{10}Be/^{9}Be Ratio Uncertainty	^{10}Be Concentration (atoms g^{-1})	^{10}Be Concentration Uncertainty (atoms g^{-1})	erosion rate (m/My)	erosion rate uncertainty (m/My)
OTT-1	21.9185	250.3	151643	4.513E-13	1.043E-14	4.468E-13	1.045E-14	3.409E-05	7.978E-03	11.5	0.982
OTT-3	23.0931	250.1	151644	6.192E-13	1.505E-14	6.147E-13	1.507E-14	4.448E-05	1.090E-04	9.01	0.778
OTT-4	21.9522	249.4	151645	5.281E-13	1.136E-14	5.236E-13	1.139E-14	3.975E-05	8.644E-03	10.3	0.875
OTT-6	21.8800	249.6	151646	4.496E-13	1.071E-14	4.450E-13	1.073E-14	3.393E-05	8.180E-03	12.2	1.04
OTT-7	21.8210	249.6	151647	3.879E-13	8.755E-15	3.834E-13	8.783E-15	2.931E-05	6.714E-03	15	1.26
TUC-1	21.9741	248.7	151649	4.686E-13	1.036E-14	4.641E-13	1.039E-14	3.510E-05	7.855E-03	11.2	0.949
TUC-2	21.9804	249.5	153400	4.655E-13	1.237E-14	4.609E-13	1.239E-14	3.496E-05	9.398E-03	11.4	0.987
TUC-3	17.2038	249.7	153401	3.980E-13	1.083E-14	3.935E-13	1.085E-14	3.817E-05	1.053E-04	10.7	0.932
TUC-4	21.9737	248.8	153402	4.414E-13	1.185E-14	4.368E-13	1.187E-14	3.305E-05	8.982E-03	12.5	1.08
TUC-5	22.0228	247.9	153403	5.457E-13	1.283E-14	5.411E-13	1.285E-14	4.070E-05	9.662E-03	10.5	0.897

*^{9}Be was added through a carrier made at University of Vermont with a concentration of 304 μg mL^{-1}.

**Isotopic analysis was conducted at PRIME Laboratory; ratios were normalized against standard 07KNSTD3110 with an assumed ratio of 2850 x 10^{-15} (Nishiizumi et al., 2007).

Sample Name	Quartz Mass (g)	Mass of ^{9}Be Added (μg)*	AMS Cathode Number	Uncorrected ^{10}Be/^{9}Be Ratio**	Uncorrected ^{10}Be/^{9}Be Ratio Uncertainty**	Background-Corrected ^{10}Be/^{9}Be Ratio	Background-Corrected ^{10}Be/^{9}Be Ratio Uncertainty	^{10}Be Concentration (atoms g^{-1})	^{10}Be Concentration Uncertainty (atoms g^{-1})	erosion rate (m/My)	erosion rate uncertainty (m/My)
OTT-5	19.9810	251.4	154577	3.887E-13	8.575E-15	3.849E-13	8.594E-15	3.236E-05	7.225E-03	12.9	1.09
OTT-8	20.0351	250.9	154578	4.480E-13	8.571E-15	4.442E-13	8.589E-15	3.716E-05	7.186E-03	11.6	0.98
TUC-6	19.9502	250.0	154579	5.351E-13	1.115E-14	5.313E-13	1.117E-14	4.449E-05	9.349E-03	9.88	0.84

*^{9}Be was added through a carrier made at University of Vermont with a concentration of 304 μg mL^{-1}.

**Isotopic analysis was conducted at PRIME Laboratory; ratios were normalized against standard 07KNSTD3110 with an assumed ratio of 2850 x 10^{-15} (Nishiizumi et al., 2007).

	erosion rate (m/My)	erosion rate uncertainty (m/My)
Otter	11.44	0.27
	11.79	0.38
Tucquan	11.03	0.39

Appendix C. MatLab Codes and Sample Datasets

The MatLab scripts, workflows, and a sample .mat dataset for Otter and Tucquan creeks are provided as an example of how the steady state channel elevations were calculated for Figures 15, 16, and 17.   These scripts use the TopoToolBox (Schwanghart and Scherler, 2014; https://topotoolbox.wordpress.com/download/)   Topography   Analysis   Kit   (TAK; https://github.com/amforte/Topographic-Analysis-Kit) assembly of MatLab tools.

The scripts created specifically for this project will be available for download after 31 October, 2020 at:

https://www.dropbox.com/s/jrhsrthoj1blaob/G18AP00061_MatLab_scripts.zip?dl=0